High-contrast gratings for integrated optoelectronics

Connie J. Chang-Hasnain* and Weijian Yang

Department of Electrical Engineering and Computer Sciences, University of California, Berkeley, California 94720, USA

*Corresponding author: cch@berkeley.edu

A new class of planar optics has emerged using subwavelength gratings with a large refractive index contrast, herein referred to as high-contrast gratings (HCGs). This seemingly simple structure lends itself to extraordinary properties, which can be designed top-down based on intuitive guidelines. The HCG is a single layer of high-index material that can be as thin as 15% of one wavelength. It can be designed to reflect or transmit nearly completely and with specific optical phase over a broad spectral range and/or various incident beam angles. We present a simple theory providing an intuitive phase selection rule to explain the extraordinary features. Our analytical results agree well not only with numerical simulations but also experimental data. The HCG has made easy fabrication of surface-normal optical devices possible, including vertical-cavity surface-emitting lasers (VCSELs), tunable VCSELs, and tunable filters. HCGs can be designed to result in high-quality-factor (Q) resonators with surface-normal output, which is promising for wafer-scale lasers and optical sensors. Spatially chirped HCGs are shown to be excellent focusing reflectors and lenses with very high numerical apertures. This field has seen rapid advances in experimental demonstrations and theoretical results. We provide an overview of the underlying new physics and the latest results of devices. © 2012 Optical Society of America

OCIS codes: 050.2770, 250.7260, 050.6624, 230.5750

High-contrast gratings for integrated optoelectronics

Connie J. Chang-Hasnain and Weijian Yang

1. Introduction

Optical gratings are among the most fundamental building blocks in optics. They are well understood in two regimes: the diffraction regime, where the grating period (Λ) is greater than the wavelength (λ) [1,2] and the deep-subwavelength regime, where the grating period is much less than the wavelength [3]. However, between these two well-known regimes lies a third, relatively unexplored regime: the near-wavelength regime, herein defined as a grating whose period is between the wavelengths inside the grating material and its surrounding media. In this regime, gratings behave radically differently and exhibit features that are not commonly attributed to gratings [4–12]. Recently, we discovered a new near-wavelength grating structure in which the high-index grating is fully surrounded by low-index materials, referred to as a high-contrast grating (HCG) [4,5]. By *fully* surrounding the high-index medium with low-index materials, many unexpected, extraordinary features were obtained. One of these features is an ultrabroadband high reflectivity (>99%). Another feature is a high-quality-factor resonance ($Q > 10^7$). Both features are surprising, because they far exceed what was observed in other subwavelength gratings, which were etched on a high-index substrate without the additional index contrast at the exiting plane [6–12].

The discovery of such surprising peculiar phenomena was first reported with a broadband ($\Delta\lambda/\lambda > 30\%$) high reflectivity (>99%) reflector for surface-normal incident light [4,5], which was demonstrated experimentally [13], and subsequently such gratings were applied as a highly reflective mirror in vertical-cavity surface-emitting lasers (VCSELs) [14]. HCGs now have been incorporated into VCSELs over a wide wavelength range, from 850 to 1550 nm, replacing the conventional distributed Bragg reflectors (DBRs) [14–28]. Monolithic, continuously tunable HCG–VCSELs have been demonstrated at 850 and 1550 nm [16–18,26]. Recently, Viktorovitch and co-workers reported an optically pumped VCSEL using two HCG mirrors, completely getting rid of DBRs [27]. Stöferle *et al.* realized a laser cavity using vertically standing HCGs, with emission in the direction parallel to the wafer surface [28]. It should be mentioned that although the high index contrast of the grating with the exiting plane is a critical differentiator, as will be discussed in Section 2, this contrast can be realized by using either a different material or a different physical design. An interesting T-shape

profile HCG is reported by Brückner *et al.* [29]. It is also interesting to point out that as the ratio of refractive indices between the grating and the surrounding media drops (even to ~1.1), the extraordinary features of high-*Q* resonance and ultrahigh reflectivity still remain, though the bandwidth of the high reflectivity is reduced significantly.

There are many other promising applications of near-wavelength HCGs in addition to replacing DBRs. First, a single-layer HCG can form a high-*Q* cavity with easy coupling with a surface-normal input/output beam [30,31]. This resonator is formed without a Fabry–Perot (FP) cavity! By varying HCG dimensions, the reflection phase can be changed, which can be used to control the VCSEL wavelength [32]. Most interestingly, a curved wave front can be obtained by locally changing each grating dimension. This leads to planar, single-layer lens and focusing reflectors with high focusing power [33,34], or arbitrary transmitted wavefront generator that can be used to split or route light [35]. The HCG can be designed to provide reflection and resonances for incident light at an oblique angle as well. A hollow-core waveguide can be made with two parallel HCGs with light guided in between [36,37]. The phase of the reflection coefficient can be designed such that slow light can be obtained in a hollow-core waveguide [38]. Two neighboring hollow-core waveguides can be completely isolated by one single HCG layer, which leads to an ultracompact optical coupler and splitter [39]. Finally, light propagation can be switched efficiently from the surface-normal direction to an in-plane index-guided waveguide and vice versa [40].

This review focuses mainly on the peculiar phenomena and applications of HCGs under surface-normal incidence, due to space limitation. We provide an in-depth analysis of the HCG, which can lead to physical insights into its extraordinary properties. We review a vast range of surface-normal device results. We show that HCGs can be easily designed by using simple guidelines, rather than requiring heavy numerical simulations through the parameter space. We believe that the HCG will be an excellent new template for chip-scale optics.

2. Physics of Near-Wavelength Gratings

To understand near-wavelength gratings, we can neither approximate nor ignore the electromagnetic field profile inside the grating. Even though fully rigorous electromagnetic solutions exist for gratings [41–43], they tend to involve heavy mathematical formulism. Recently, Chang-Hasnain and co-workers published a simple analytic formulism to explain the broadband reflection and resonance [44–46]. Independently, Lalanne *et al.* published a quasi-analytical method using coupled Bloch modes [47] with a rather similar formulism. In this section, we will provide a complete and in-depth review of the formulism and its implication.

Figure 1 shows the schematic of a generic HCG, with air as the low-index medium on top and between the grating bars, a second low-index material beneath the bars, and an incident plane wave at an oblique angle. The HCG is polarization sensitive by its nature of one-dimensional (1D) periodicity. Incident beams with *E*-field polarization along and perpendicular to the grating bars are referred to as transverse electric
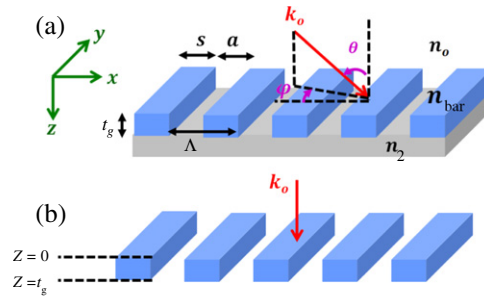
(a) Generic HCG structure. The grating comprises simple dielectric bars with high refractive index n_{bar}, surrounded by a low-index medium n_o. A second low-index material n_2 is beneath the bars. The plane wave is incident from the top at an oblique angle. Λ, HCG period; s, bar width; a, air gap width; t_g, HCG thickness. For surface-normal ($\theta = 0$) TE incidence, $\varphi = 0$, and the electrical field is parallel to the grating bars; whereas for TM, $\varphi = \pi/2$, and the electrical field is perpendicular to the grating bars. (b) The HCG conditions that will be discussed in this paper are surface normal incidence, $n_o = 1$, $n_{bar} = 1.2$–3.6, $n_2 = 1$.

(TE) and transverse magnetic (TM) polarizations, respectively. We also show two incident characteristic angles, θ and φ, the incident directions between the incident beam and the y–z and the x–z planes, respectively.

To explain the basic principle, we will first simplify the structure by (1) considering the second low-index material as air, (2) ignoring the substrate under the second low-index material, and (3) considering only the surface-normal incident plane wave ($\theta = 0$) with TE ($\varphi = 0$) or TM polarization ($\varphi = \pi/2$). The main design parameters include the index of refraction of the high-index materials n_{bar}, grating period Λ, grating thickness t_g and grating bar width s. The grating duty cycle (η) is defined as the ratio of the width of the high-index material with period, i.e., $\eta = s/\Lambda$.

In Subsection 2.1, we first outline the underlying physics, to be followed by analytical formulism in Subsection 2.2 and phase selection rules in Subsection 2.3.

2.1. Overview of the Underlying Principles

The grating bars can be considered as merely a periodic array of waveguides along the z direction. Upon plane wave incidence, depending on wavelength and grating dimensions, a few waveguide array modes are excited. Because of the large index contrast and near-wavelength dimensions, there exists a wide wavelength range where only two modes have real propagation constants in the z direction and, hence, carry energy. This is the regime of interest. The two modes then depart from the grating input plane ($z = 0$) and propagate downward ($+z$ direction) to the grating output plane ($z = t_g$), and then reflect back up. The higher-order modes are typically below cutoff and have the form of evanescent surface-bound waves.

After propagating through the HCG thickness, each propagating mode accumulates a different phase. At the exiting plane, owing to a strong mismatch with the exiting plane wave, the waveguide modes not only reflect back to themselves but also couple into each other. As the modes propagate and return to the input plane, similar mode coupling occurs. Following the modes through one round trip, the reflectivity solution can be attained. Note that, at both input and exiting planes, the waveguide modes also transmit out to air (or, more generally, the low-index media). However, due to HCG's subwavelength period in air, only the zeroth diffraction order carries energy in reflection and transmission, which are plane waves. This is perhaps the most important part that contributes to the HCG properties. The HCG thickness determines the phase accumulated by the modes and controls their interference, making it one of the most important design parameters.

To obtain high reflection, the HCG thickness should be chosen such that a destructive interference is obtained at the exit plane, which cancels transmission. For full transmission, on the other hand, the thickness should be chosen such that the interference is well matched with the input plane wave at the input plane. On the other hand, when a constructive interference is obtained at both input and exit planes, a high-Q resonator results. Here, destructive interference does not mean that the fields are zero everywhere. Rather, it means that the spatial mode overlap with the transmitted plane wave is 0, yielding a zero transmission coefficient. This prevents optical power from being launched into a transmissive propagating wave, and thus causes full reflection. A matched interference at the input plane means the spatial mode overlap with input plane wave is 1, making a complete impedance match, and thus cancelling any reflection. For a high-Q resonator, the HCG array modes couple strongly to one another and become self-sustaining after each round trip. The resonator can thus reach high Q without mirrors—another unique and distinct feature for HCG.

Three main phenomena observed in surface-normal HCGs are shown in Fig. 2, obtained by numerical simulation using rigorous coupled wave analysis (RCWA), a broadly accepted method that uses a matrix formalism to analytically solve for the reflected and transmitted diffraction orders of planar gratings [41]. The surface-normal reflectivity spectrum of *resonant gratings* (in red) exhibits several high-Q resonances, characterized by very sharp transitions from 0 to ~100% reflectivity and vice versa, e.g., 1.682 and 1.773 μm in Fig. 2(a), marked by two arrows. Figure 2(b) shows the reflectivity spectrum of the *broadband reflector* (in blue), which exhibits reflectivity above 99% across a large bandwidth. Finally, broadband transmission (in green) can be obtained with a different set of HCG parameters, also shown in Fig. 2(b). In the next subsection, we develop an analytical solution for the HCG. The analytical solution is compared against numerical simulations using RCWA and the finite-difference time-domain (FDTD) method. We found excellent agreement among all three.
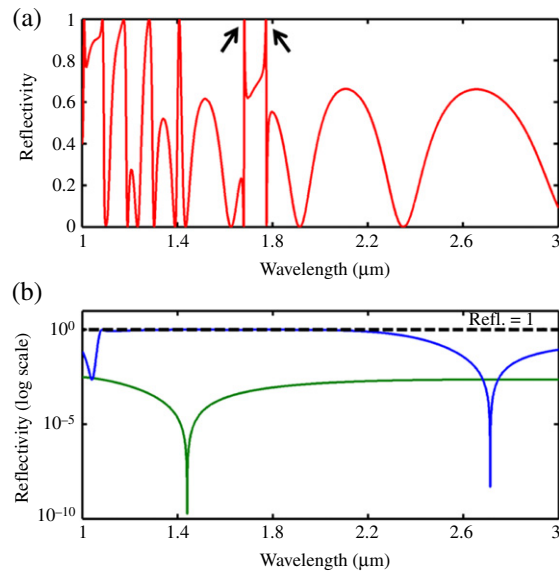
Examples of three types of extraordinary reflectivity/transmission feature: (a) high-Q resonances (red) and (b) broadband high reflection (blue), and broadband high transmission (green). The high-Q resonances are characterized by very sharp transitions from 0 to ~100% reflectivity and vice versa, e.g., 1.682 and 1.773 μm, as labeled by the black arrows. For the broadband high-reflection case, the 99% reflection bandwidth is 578 nm (from 1.344 to 1.922 μm); this corresponds to $\triangle\lambda/\lambda \sim 35\%$. The dashed black line indicates the reflectivity equal to one. For the broadband high-transmission case, the transmission is larger than 99.68% over a broad spectrum, not limited to the 1–3 μm shown in the figure. The HCG parameters for the three different cases are high-Q resonances, $\Lambda = 0.716$ μm, $t_g = 1.494$ μm, $\eta = 0.70$, TE-polarized light; broadband high reflection, $\Lambda = 0.77$ μm, $t_g = 0.455$ μm, $\eta = 0.76$, TM-polarized light; and broadband high transmission, $\Lambda = 0.8$ μm, $t_g = 0.6$ μm, $\eta = 0.1$, TM polarized light. $n_{\mathrm{bar}} = 3.48$ for all three cases.

2.2. Analytical Formulation

2.2a. TM-Polarized Surface-Normal Incidence

For simplicity, we focus on a TM-polarized, surface-normal plane wave as incident light. The HCG is assumed to be infinite in y and infinitely periodic in x. The solution is thus two-dimensional (2D, $\partial/\partial y = 0$). We consider three regions, separated by the HCG input plane $z = 0$ and output/exit plane $z = t_g$. In region I, $z < 0$, there are incoming plane wave and reflected waves. In region II, $0 < z < t_g$, the solutions are modes of a periodic array of slab waveguides. In region III, $z > t_g$, there exist only the transmitted waves. For simplicity, all low-index media have refractive index of 1. We will keep track of the lateral (x, y) field components only, since the longitudinal (z) field component can be easily derived from the lateral components, depicted by Fig. 3.

The magnetic and electric fields in region I, $H_y^{\mathrm{I}}(x, z)$ and $E_x^{\mathrm{I}}(x, z)$, respectively, are expressed as the sum of the incident plane wave and

Figure 3
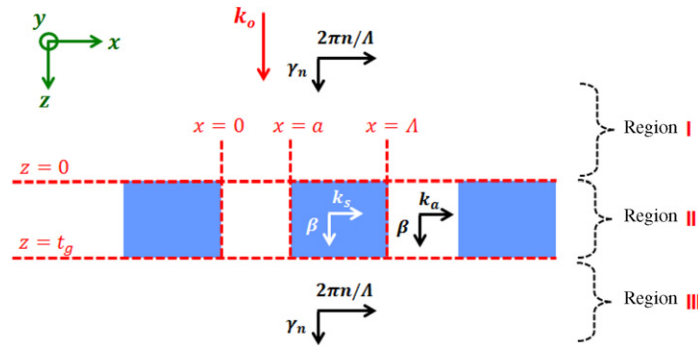
Nomenclature for Eqs. (1a)–(1e): The HCG input plane is $z = 0$, and the output/exit plane is $z = t_g$. In region II, k_a and k_s are the x wavenumbers in the air gaps and in the grating bars, respectively. The z wavenumber β is the same in both the air gaps and the bars. The x wavenumber outside the grating (regions I and III) is determined by the grating periodicity: $2\pi n/\Lambda$, where $n = 0, 1, 2, \ldots$.

multiple reflected modes, whose magnetic field, electric field, reflection coefficient, and propagation constant are $\mathcal{H}^I_{y,n}(x)$, $\mathcal{E}^I_{x,n}(x)$, r_n, and γ_n, respectively, where $n = 0, 1, 2, \ldots$ is the reflected mode number:

$$H^I_y(x, z) = e^{-jk_0 z} - \sum_{n=0}^{\infty} r_n \mathcal{H}^I_{y,n}(x) e^{+j\gamma_n z}, \quad z < 0,$$

$$E^I_x(x, z) = \sqrt{\frac{\mu_0}{\varepsilon_0}} e^{-jk_0 z} + \sum_{n=0}^{\infty} r_n \mathcal{E}^I_{x,n}(x) e^{+j\gamma_n z}, \quad z < 0, \qquad (1a)$$

$$\mathcal{H}^I_{y,n}(x) = \cos[(2n\pi/\Lambda)(x - a/2)], \qquad \mathcal{E}^I_{x,n}(x) = (\gamma_n/k_0)\sqrt{\frac{\mu_0}{\varepsilon_0}} \mathcal{H}^I_{y,n}(x),$$

$$(1b)$$

$$k_0 = \frac{2\pi}{\lambda}, \qquad \gamma_n^2 = k_0^2 - (2n\pi/\Lambda)^2. \qquad (1c)$$

Here μ_0 and ε_0 are the vacuum permeability and vacuum permittivity, respectively. As is evident from Eq. (1c), in subwavelength gratings ($\Lambda < \lambda$), only the zeroth diffraction order is propagating (γ_0 is real), while the higher orders are all evanescent (γ_1, γ_2, etc. are imaginary).

In Eq. (1b), we have chosen the air-gap center ($x = a/2$) as a symmetry plane for all modes in region I. Alternatively, the solution could be written with the center of a grating bar (e.g., $x = (a + \Lambda)/2$) as the symmetry plane. The end results will be the same (not shown here). In addition, considering surface normal incidence means that the solution above has no preferred direction among $+x$ and $-x$, and therefore the modes in Eq. (1b) have a standing wave (cosine) lateral profile. The lateral symmetry in Eq. (1b) is even (cosine) rather than odd (sine), because the incident plane wave [Eq. (1a)] has a laterally constant profile, and thus it can only excite laterally even modes. The same considerations will be applied to region II and III solutions.

The transmitted mode profiles for region III are given by Eq. (1d):

$$H_y^{\mathrm{III}}(x, z) = \sum_{n=0}^{\infty} \tau_n \mathcal{H}_{y,n}^{\mathrm{III}}(x) e^{-j\gamma_n(z-t_g)}, \quad z > t_g,$$

$$E_x^{\mathrm{III}}(x, z) = \sum_{n=0}^{\infty} \tau_n \mathcal{E}_{x,n}^{\mathrm{III}}(x) e^{-j\gamma_n(z-t_g)}, \quad z > t_g.$$

$$\mathcal{H}_{y,n}^{\mathrm{III}}(x) = \mathcal{H}_{y,n}^{\mathrm{I}}(x) \quad \text{and} \quad \mathcal{E}_{x,n}^{\mathrm{III}}(x) = \mathcal{E}_{x,n}^{\mathrm{I}}(x). \tag{1d}$$

The incident wave in region I can be expressed as a vector $(1 \quad 0 \quad 0 \quad \ldots)^T$. The HCG reflectivity matrix $\mathbf{R}$ and transmission matrix $\mathbf{T}$ are expressed with coefficients of the reflected and transmitted modes r_n and τ_n, respectively:

$$\mathbf{r} \equiv (r_0 \quad r_1 \quad r_2 \quad \ldots)^T \equiv \mathbf{R} (1 \quad 0 \quad 0 \quad \ldots)^T, \tag{1e}$$

$$\boldsymbol{\tau} \equiv (\tau_0 \quad \tau_1 \quad \tau_2 \quad \ldots)^T \equiv \mathbf{T} (1 \quad 0 \quad 0 \quad \ldots)^T. \tag{1f}$$

The modes in region II comprise m waveguide-array modes ($m = 0, 1, 2, \ldots$) with lateral (x) magnetic and electric fields of $\mathcal{H}_{y,m}^{\mathrm{II}}(x)$ and $\mathcal{E}_{x,m}^{\mathrm{II}}(x)$, respectively, and propagating constants of β_m in the longitudinal direction (z). The forward ($+z$) and backward ($-z$) propagating components have coefficients of a_m and b_m, respectively:

$$H_y^{\mathrm{II}}(x, z) = \sum_{m=0}^{\infty} \mathcal{H}_{y,m}^{\mathrm{II}}(x) [a_m e^{-j\beta_m(z-t_g)} - b_m e^{+j\beta_m(z-t_g)}],$$

$$0 < z < t_g,$$

$$E_x^{\mathrm{II}}(x, z) = \sum_{m=0}^{\infty} \mathcal{E}_{x,m}^{\mathrm{II}}(x) [a_m e^{-j\beta_m(z-t_g)} + b_m e^{+j\beta_m(z-t_g)}],$$

$$0 < z < t_g, \tag{2a}$$

$$\mathcal{H}_{y,m}^{\mathrm{II}}(x) = A \cos[k_{a,m}(x - a/2)] + B \sin[k_{a,m}(x - a/2)], \quad 0 < x < a,$$

$$\mathcal{E}_{x,m}^{\mathrm{II}}(x) = (\beta_m/k_0)\sqrt{\frac{\mu_0}{\varepsilon_0}} \mathcal{H}_{y,m}^{\mathrm{II}}(x), \quad 0 < x < a,$$

$$\mathcal{H}_{y,m}^{\mathrm{II}}(x) = C \cos\{k_{s,m}[x - (a + \Lambda)/2]\} + D \sin\{k_{s,m}[x - (a + \Lambda)/2]\},$$

$$a < x < \Lambda,$$

$$\mathcal{E}_{x,m}^{\mathrm{II}}(x) = n_{\mathrm{bar}}^{-2}(\beta_m/k_0)\sqrt{\frac{\mu_0}{\varepsilon_0}} \mathcal{H}_{y,m}^{\mathrm{II}}(x), \quad a < x < \Lambda. \tag{2b}$$

Equation (2b) is a general solution including both sine functions (odd modes) and cosine functions (even modes). Here, k_a and k_s are the lateral wavenumbers inside air gaps and grating bars, respectively. For an incident wave with surface-normal incidence, $\mathcal{H}_{y,m}^{\mathrm{II}}(x)$ and $\mathcal{E}_{x,m}^{\mathrm{II}}(x)$ are even functions, and thus $B = D = 0$. By matching the boundary conditions at $x = a$ and the following periodic boundary conditions,

$$\mathcal{H}_{y,m}^{\mathrm{II}}(x) = \mathcal{H}_{y,m}^{\mathrm{II}}(x + l\Lambda), \quad l \text{ is an integer,}$$

$$\mathcal{E}_{x,m}^{\mathrm{II}}(x) = \mathcal{E}_{x,m}^{\mathrm{II}}(x + l\Lambda), \quad l \text{ is an integer,} \tag{2c}$$

one can solve for A and C. Thus, for surface normal incidence,

$$A = \cos(k_{s,m}s/2),$$
$$C = \cos(k_{a,m}a/2),$$
$$B = 0,$$
$$D = 0,$$
$$\mathcal{H}^{\mathrm{II}}_{y,m}(x) = \mathcal{E}^{\mathrm{II}}_{x,m}(x) = 0 \quad \text{when } m = 1, 3, 5, \ldots. \tag{2d}$$

Note that one should always include the sine functions for oblique incident angle.

The longitudinal wave number β_m in Eq. (2a) is given by

$$\beta_m^2 = (2\pi/\lambda)^2 - k_{a,m}^2 = (2\pi n_{\mathrm{bar}}/\lambda)^2 - k_{s,m}^2. \tag{2e}$$

Thus

$$k_{s,m}^2 - k_{a,m}^2 = (2\pi/\lambda)^2 \left(n_{\mathrm{bar}}^2 - 1\right). \tag{2f}$$

The characteristic equation between the lateral wavenumbers k_a and k_s can be solved by matching the boundary conditions at $x = 0$ and $x = a$ to describe the waveguide array:

$$n_{\mathrm{bar}}^{-2} k_{s,m} \tan\left(k_{s,m}s/2\right) = -k_{a,m} \tan\left(k_{a,m}a/2\right). \tag{2g}$$

To see that Eq. (2g) approaches the characteristic equation of a slab waveguide, we can simply push period Λ, and consequently a, to infinity. Equation (2g) cannot converge unless $k_{a,m}$ is imaginary, in which case $\tan(k_{a,m}a/2) \rightarrow i$. This becomes exactly the dispersion relation of an ordinary slab waveguide [48].

The ω–β relations ($\omega = 2\pi c/\lambda$) resulting from Eqs. (2e)–(2g) are essentially waveguide array ω–β diagrams, which are independent of HCG thickness t_g, and are plotted in Fig. 4. The dispersion curves between the air light line, $\beta = \omega/c$, and the dielectric light line, $\beta = \omega n_{\mathrm{bar}}/c$, indeed resemble those of an ordinary slab waveguide [48]. Here, we see several trends that are typical of waveguides: (1) as frequency increases, more and more modes exist; (2) except for the fundamental mode, there is a cutoff frequency (denoted ω_{c2}, ω_{c4}, etc.) for each higher-order mode (the cutoff condition being $\beta = 0$); and (3) the higher the mode order, the higher the cutoff frequency (the shorter the cutoff wavelength). Similar to the notation in the ordinary slab waveguide, we denote the waveguide array modes as TE_0, TE_2, TE_4, etc. for TE light; and TM_0, TM_2, TM_4, etc. for TM light. For surface normal incidence, only even modes can be excited. For the general oblique angle incidence case, odd modes ($\mathrm{TE}_1/\mathrm{TM}_1$, $\mathrm{TE}_3/\mathrm{TM}_3$ etc.) will need to be considered.

One main difference from ordinary slab waveguides stands out: the HCG has a discrete set of modes for $\beta < \omega/c$, in contrast to the continuum of radiation modes observed for a slab waveguide. This discretization is a direct consequence of the grating periodicity. The cutoff frequencies in Fig. 4 are important, since they determine the regime in which the grating operates. As will be shown subsequently, the extraordinary features

Figure 4
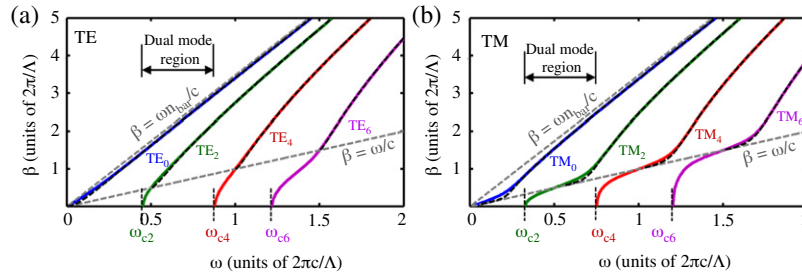
Dispersion curves of a single slab waveguide (dashed) and waveguide array modes (solid), for the same bar width s and index n_{bar}, β being the z wavenumbers. Between the two light lines, the dispersion curves of the waveguide array modes are nearly identical to those of the single slab waveguide [48]. Below the air light line ($\beta < \omega/c$) there is a discrete set of modes due to subwavelength grating periodicity. ω_{c2} and ω_{c4} are the cutoffs of the TE_2/TM_2 and the TE_4/TM_4 modes, respectively, and between them the grating operates at a dual-mode regime. For HCG with surface-normal incidence, we only need to consider the even modes. The TE condition is plotted in (a), and TM in (b). In this calculation, $\eta = 0.6$, $n_{bar} = 3.48$.

discussed in the introduction are observed primarily in the regime where exactly two modes exist, hereinafter called the "dual-mode" regime (e.g., TE_0 and TE_2, or TM_0 and TM_2).

One distinguished difference between TE and TM in ω–β diagrams is located at their crossing with the air light line. For TE light, the slopes of the ω–β curve are nearly constants, whereas for TM light, the slopes change significantly near the air light line crossings. This difference contributes largely to the different properties of TE and TM HCGs, as will be discussed below.

Based on the mode profiles for regions I–III described in Eqs. (1)–(2), we can now calculate the HCG reflectivity by matching the boundary conditions of H_y and E_x at the HCG output plane $z = t_g$ and input plane $z = 0$. To gain physical insight, we first have an overview on the mode behaviors in region II, before proceeding the calculation. As described in Eq. (2a), once the waveguide array modes are excited inside the HCG (region II), they would propagate along the HCG in $+z$ direction. When they hit the HCG output plane at $z = t_g$, they are reflected and at the same time scattered to each other. The same happens when these modes return to the HCG input plane at $z = 0$. We thus define two vectors, $\boldsymbol{a}$ and $\boldsymbol{b}$, to describe the coefficients of the different modes propagating in the $+z$ and $-z$ direction. Note that $\boldsymbol{a}$ and $\boldsymbol{b}$ are independent of x and z:

$$\boldsymbol{a} \equiv \begin{pmatrix} a_0 & a_1 & a_2 & \ldots \end{pmatrix}^T, \qquad \boldsymbol{b} \equiv \begin{pmatrix} b_0 & b_1 & b_2 & \ldots \end{pmatrix}^T. \qquad (3a)$$

The relationship between $\boldsymbol{a}$ and $\boldsymbol{b}$ can be described by a reflection matrix $\boldsymbol{\rho}$, such that

$$\boldsymbol{b} \equiv \boldsymbol{\rho}\boldsymbol{a}. \qquad (3b)$$

Note the reflection matrix $\boldsymbol{\rho}$ in Eq. (3b) is typically nondiagonal, which means that the HCG modes in region II couple into each other during the reflection. This does not contradict the orthogonality of the modes in region II, since the reflection involves interaction with the external modes of region III, which are not orthogonal to the modes in region II.

We further define a propagation matrix $\boldsymbol{\varphi}$ to describe the accumulated phase when each mode propagates from $z = 0$ to $z = t_g$. Matrix $\boldsymbol{\varphi}$ is a diagonal matrix, since the different modes are orthogonal to each other and thus would not couple to each other during propagation:

$$\boldsymbol{\varphi}_{n,m} = \begin{cases} e^{-j\beta_m t_g} & \text{for } n = m \\ 0 & \text{for } n \neq m \end{cases}. \tag{3c}$$

By matching the boundary conditions of electromagnetic field at the HCG input and output planes, matrix $\boldsymbol{\rho}$ can be calculated, and thus $\mathbf{R}$ and $\mathbf{T}$. As will be discussed below, it is $\boldsymbol{\varphi}$ (mode propagation inside HCG) and $\boldsymbol{\rho}$ (mode interaction at HCG input and output plane) that give rise to the rich properties of HCGs.

Next, we first match the boundary conditions that H_y and E_x are continuous at the HCG *output* plane, $z = t_g$:

$$\sum_{n=0}^{\infty} \tau_n \mathcal{H}_{y,n}^{\mathrm{III}}(x) = \sum_{m=0}^{\infty} \mathcal{H}_{y,m}^{\mathrm{II}}(x)(a_m - b_m),$$

$$\sum_{n=0}^{\infty} \tau_n \mathcal{E}_{x,n}^{\mathrm{III}}(x) = \sum_{m=0}^{\infty} \mathcal{E}_{x,m}^{\mathrm{II}}(x)(a_m + b_m). \tag{4a}$$

By performing a Fourier overlap integral on both sides of Eq. (4a), we can express the transmitted coefficients τ_n in terms of the overlaps between the lateral (x) magnetic field profiles $\mathcal{H}_{y,m}^{\mathrm{II}}(x)$ and $\mathcal{H}_{y,n}^{\mathrm{III}}(x)$:

$$\tau_n \Lambda^{-1} \int_0^\Lambda [\mathcal{H}_{y,n}^{\mathrm{III}}(x)]^2 dx = \sum_{m=0}^{\infty} (a_m - b_m)\Lambda^{-1} \int_0^\Lambda \mathcal{H}_{y,m}^{\mathrm{II}}(x)\mathcal{H}_{y,n}^{\mathrm{III}}(x)dx, \tag{4b}$$

$$\tau_n \Lambda^{-1} \int_0^\Lambda [\mathcal{E}_{x,n}^{\mathrm{III}}(x)]^2 dx = \sum_{m=0}^{\infty} (a_m + b_m)\Lambda^{-1} \int_0^\Lambda \mathcal{E}_{x,m}^{\mathrm{II}}(x)\mathcal{E}_{x,n}^{\mathrm{III}}(x)dx. \tag{4c}$$

Next we define the overlap matrices $\mathbf{H}$ and $\mathbf{E}$ (both are unitless), for the magnetic and electric field profiles, respectively, based on Eqs. (4b) and (4c), and then rewrite Eqs. (4b) and (4c) in matrix-vector format:

$$\mathbf{H}_{n,m} = \Lambda^{-1}(2 - \delta_{n,0}) \int_0^\Lambda \mathcal{H}_{y,m}^{\mathrm{II}}(x)\mathcal{H}_{y,n}^{\mathrm{III}}(x)dx,$$

$$\mathbf{E}_{n,m} = \Lambda^{-1}(2 - \delta_{n,0}) \left(\sqrt{\frac{\mu_0}{\varepsilon_0}}\gamma_n/k_0\right)^{-2} \int_0^\Lambda \mathcal{E}_{x,m}^{\mathrm{II}}(x)\mathcal{E}_{x,n}^{\mathrm{III}}(x)dx,$$

$$\boldsymbol{\tau} = \mathbf{H}(\boldsymbol{a} - \boldsymbol{b}) = \mathbf{E}(\boldsymbol{a} + \boldsymbol{b}). \tag{5a}$$

The closed form of $\mathbf{H}_{n,m}$ and $\mathbf{E}_{n,m}$ can be derived with Eqs. (1b), (1d), (2b), and (2d). See Appendix A for the results.

Equation (5a) can be rewritten as follows, using the definition of matrix $\boldsymbol{\rho}$ in Eq. (3b):

$$\boldsymbol{\tau} = \mathbf{H}(\mathbf{I} - \boldsymbol{\rho})\boldsymbol{a} = \mathbf{E}(\mathbf{I} + \boldsymbol{\rho})\boldsymbol{a}. \tag{5b}$$

Since Eq. (5b) holds for every coefficient vector $\boldsymbol{a}$, we can now derive the reflection matrix $\boldsymbol{\rho}$ as a function of the overlap matrices $\mathbf{E}$ and $\mathbf{H}$:

$$\mathbf{H}(\mathbf{I} - \boldsymbol{\rho}) = \mathbf{E}(\mathbf{I} + \boldsymbol{\rho}) \Rightarrow \boldsymbol{\rho} = (\mathbf{I} + \mathbf{H}^{-1}\mathbf{E})^{-1}(\mathbf{I} - \mathbf{H}^{-1}\mathbf{E}). \tag{6}$$

Having matched the boundary conditions at the HCG output plane ($z = t_g$), we now repeat the steps in Eqs. (4) in order to match the boundary conditions at the HCG input plane ($z = 0$):

$$\sum_{n=0}^{\infty}(\delta_{n,0} - r_n)\mathcal{H}_{y,n}^{\mathrm{I}}(x) = \sum_{m=0}^{\infty}\mathcal{H}_{y,m}^{\mathrm{II}}(x)[a_m e^{+j\beta_m t_g} - b_m e^{-j\beta_m t_g}],$$

$$\sum_{n=0}^{\infty}(\delta_{n,0} + r_n)\mathcal{E}_{x,n}^{\mathrm{I}}(x) = \sum_{m=0}^{\infty}\mathcal{E}_{x,m}^{\mathrm{II}}(x)[a_m e^{+j\beta_m t_g} + b_m e^{-j\beta_m t_g}]. \tag{7a}$$

For simplicity, this time we omit the details shown in Eqs. (4) and jump straight to the final equation:

$$(\mathbf{I} - \mathbf{R})^{-1}\mathbf{H}(\mathbf{I} - \boldsymbol{\varphi}\boldsymbol{\rho}\boldsymbol{\varphi}) = (\mathbf{I} + \mathbf{R})^{-1}\mathbf{E}(\mathbf{I} + \boldsymbol{\varphi}\boldsymbol{\rho}\boldsymbol{\varphi}). \tag{7b}$$

By rearranging Eq. (7b), we can implicitly express the HCG reflectivity matrix $\mathbf{R}$ in terms of the matrices $\mathbf{E}$, $\mathbf{H}$, $\boldsymbol{\rho}$, and $\boldsymbol{\varphi}$:

$$\mathbf{E}(\mathbf{I} + \boldsymbol{\varphi}\boldsymbol{\rho}\boldsymbol{\varphi})(\mathbf{I} - \boldsymbol{\varphi}\boldsymbol{\rho}\boldsymbol{\varphi})^{-1}\mathbf{H}^{-1} = (\mathbf{I} + \mathbf{R})(\mathbf{I} - \mathbf{R})^{-1} \triangleq \mathbf{Z_{in}}. \tag{7c}$$

This definition of input impedance matrix $\mathbf{Z_{in}}$ resembles that used in transmission lines [49], with only the difference of the latter being scalar. Using Eq. (7c), the HCG reflectivity matrix $\mathbf{R}$ can finally be calculated, resulting in an equation very common in transmission line theory:

$$\mathbf{R} = (\mathbf{Z_{in}} + \mathbf{I})^{-1}(\mathbf{Z_{in}} - \mathbf{I}), \quad \text{where } \mathbf{Z_{in}} = \mathbf{E}(\mathbf{I} + \boldsymbol{\varphi}\boldsymbol{\rho}\boldsymbol{\varphi})(\mathbf{I} - \boldsymbol{\varphi}\boldsymbol{\rho}\boldsymbol{\varphi})^{-1}\mathbf{H}^{-1}. \tag{8a}$$

Similarly, the HCG transmission matrix $\mathbf{T}$ can be shown to be

$$\mathbf{T} = 2\mathbf{E}(\mathbf{I} + \boldsymbol{\rho})\boldsymbol{\varphi}[(\mathbf{Z_{in}^{-1}} + \mathbf{I})\mathbf{E}(\mathbf{I} + \boldsymbol{\varphi}\boldsymbol{\rho}\boldsymbol{\varphi})]^{-1}. \tag{8b}$$

Finally, given $\Lambda < \lambda$, the HCG reflectivity and transmission are simply $|\mathbf{R}_{00}|^2$ and $|\mathbf{T}_{00}|^2$, where

$$|\mathbf{R}_{00}|^2 + |\mathbf{T}_{00}|^2 \equiv 1. \tag{9}$$

Since subwavelength gratings do not have diffraction orders other than the zeroth order, all power that is not transmitted through the zeroth diffraction order is reflected back. This fact is essential for the design of high-reflectivity gratings, since high reflectivity can be achieved by merely cancelling the zeroth transmissive diffraction order (i.e., $\tau_0 = 0$).

Table 1. Differences between TM and TE Polarizations of Incidence

Substitutions		Equation[a]												
TM	TE	(1a)	(1b)	(1d)	(2a)	(2b)	(2c)	(2d)	(2g)	(4a)	(4b)	(4c)	(5a)	(7a)
H_y	H_x	✓		✓	✓									
E_x	E_y	✓		✓	✓									
$\mathcal{H}_y$	$\mathcal{H}_x$	✓	✓	✓	✓	✓	✓	✓		✓	✓		✓	✓
$\mathcal{E}_x$	$\mathcal{E}_y$	✓	✓	✓	✓	✓	✓	✓		✓		✓	✓	✓
n_{bar}^{-2}	1					✓			✓					
β_m/k_0	$-k_0/\beta_m$					✓								
γ_n/k_0	$-k_0/\gamma_n$			✓									✓	

[a] Check marks indicate the changes required for the equation. Equations not listed in this table require no changes.

Figure 5
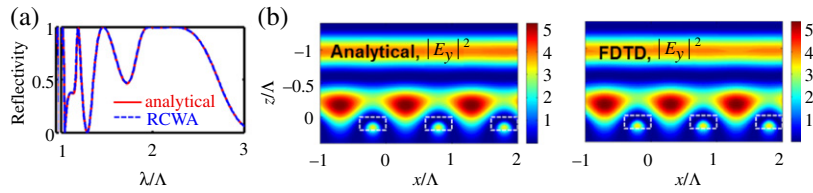
Excellent agreement between analytical solutions and commercial numerical simulation on HCG reflectivity and field intensity profile. (a) Comparison of HCG reflectivity spectrum calculated by analytical solution (red) and RCWA (blue). HCG parameters are $t_g/\Lambda = 0.627$, $\eta = 0.62$, $n_{\mathrm{bar}} = 3.214$, and TM polarization. (b) Comparison of HCG field intensity profile ($|\mathbf{E}_y|^2$) calculated by analytical solution and FDTD. HCG parameters are $\lambda/\Lambda = 1.509$, $t_g/\Lambda = 0.2$, $\eta = 0.4$, $n_{\mathrm{bar}} = 3.48$, and TE polarization. The white boxes indicate the HCG bars.

2.2b. TE-Polarized Surface-Normal Incidence

The analysis for TE-polarized incidence follows the same steps as in Subsection 2.2a. The only differences are summarized in Table 1. The reason for the differences is simple: the TM solution relies largely on the Maxwell–Ampère equation, $\nabla \times \vec{H} = j\omega\varepsilon_0\varepsilon_r\vec{E}$, whereas the TE solution relies largely on the Maxwell–Faraday equation, $\nabla \times \vec{E} = -j\omega\mu\vec{H}$. The lack of ε_r in Faraday's equation explains why n_{bar}^{-2} is replaced by 1, and the minus sign in Faraday's equation explains the minus sign in the last two entries of Table 1. The inversion of the wavenumber ratios in the last two entries of Table 1 is also a common difference between TM and TE modes in waveguides.

2.2c. Comparison with Numerical Simulations

The analytical solutions are compared with the numerical simulation using RCWA and FDTD. Figure 5(a) presents the HCG reflectivity spectrum calculated by the analytical solution and RCWA. Figure 5(b) shows the field intensity profile of an HCG reflector using the analytical solution and FDTD. Excellent agreements are obtained.

2.3. Phase Selection Rules of High-Contrast Gratings

The waveguide array structure in the x direction hosts several propagation modes in region II, as seen in the ω–β diagram in Fig. 4. These modes do not interact with each other, as defined in their orthogonality. When the HCG's two boundaries are brought into the z direction, these modes are confined in the z direction, and thus a cavity is formed. At the HCG's input and output plane, these modes (1) outcouple to the transmissive plane wave in regions I and III; (2) exchange energy with evanescent waves in regions I and III; (3) reflect to themselves; (4) couple to each other. All of these effects are lumped into the $\boldsymbol{\rho}$ matrix—it alters the magnitude as well as the phase of each waveguide array mode. When these modes interfere with each other at the input/output planes, interesting phenomena will happen. Note that the $\boldsymbol{\rho}$ matrix is not Hermitian, simply because it only relates the modes in region II, and the system is an open system with outcoupling to plane waves. From the perspective of a cavity, one can envision that the $\boldsymbol{\varphi}$ and $\boldsymbol{\rho}$ matrices dominantly determine the HCG properties.

To better understand the HCG as a cavity, we plot the reflectivity contour map versus normalized wavelength and grating thickness (both by Λ) for a surface-normal incident TE-plane wave onto an HCG, shown in Fig. 6. A fascinatingly well-behaved, highly ordered, checkerboard pattern reveals its strong property dependence on both wavelength and HCG thickness, which indicates an interference effect. This checkerboard pattern is particularly pronounced in the *dual-mode* regime for wavelengths between λ_{c2} and λ_{c4} (cutoff wavelengths of the TE$_2$ and TE$_4$ waveguide array modes, respectively). We further note that half of the "checkerboard" spaces have high reflectivity (dark red contour), while the other half have lower reflectivity (dark blue contour). This interesting phenomenon relates to the interference of the two modes at the HCG output plane. We will delay the discussion of this until the next subsection.

For wavelengths longer than λ_{c2}, only one grating mode exists, and the grating operates in the deep-subwavelength regime, behaving as a quasi-uniform layer. The reflectivity contour is governed by a simple FP mechanism, which is recognizable by the (quasi) linear bands in Fig. 6(a). For wavelengths shorter than λ_{c4}, on the other hand, more and more modes emerge, and the reflectivity contour shapes become less and less ordered. Below the subwavelength limit ($\lambda < \Lambda$), the grating enters the *diffraction regime*, where higher diffraction orders emerge outside the grating and reflectivity is greatly reduced.

The intricate checkerboard contour-shapes of the dual-mode regime in Fig. 6(a) suggest a strong underlying order related to the HCG cavity, which is characterized by the $\boldsymbol{\varphi}$ and $\boldsymbol{\rho}$ matrices. In the dual-mode regime, the sizes of $\boldsymbol{\varphi}$ and $\boldsymbol{\rho}$ are essentially shrunk to 2×2. We designate $2\psi_m$ as the phases accumulated by the supermode m, eigensolution of $\boldsymbol{\rho\varphi}$ as a mixture of the original waveguide array modes, after one round trip through the grating. ψ_m is given by

$$\psi_m \equiv \text{phase } (m\text{th eigenvalue of } \boldsymbol{\rho\varphi}). \tag{10}$$
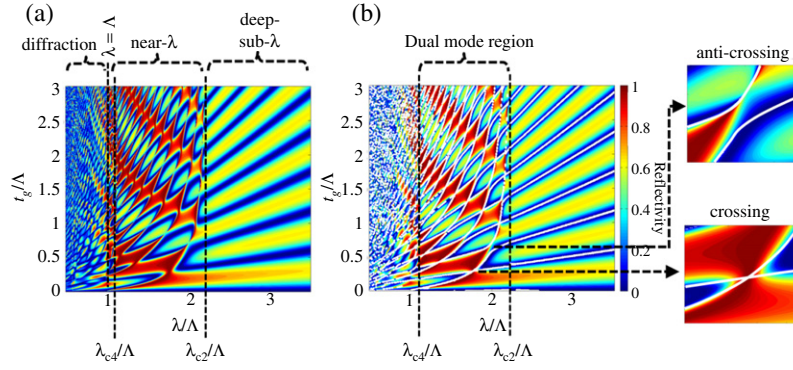
Figure 6

(a) Reflectivity contour of an HCG as a function of wavelength and grating thickness. The incident wave has a TE-polarized, surface-normal incidence. The mode cutoffs (λ_{c2}, λ_{c4}) and the first-order diffraction cutoff line $\lambda = \Lambda$ are marked to clearly illustrate the differences of the three wavelength regimes: deep-subwavelength, near-wavelength, and diffraction. (b) Analytical solutions of FP resonance conditions of the individual modes [Eq. (11)], shown by the white curves, superimposed on the reflectivity contour in (a). Excellent agreement is obtained between the analytic solutions and the simulation results. The insets show examples of an anticrossing and a crossing of the FP resonance lines (white curves). HCG parameters are $\eta = 0.6$, $n_{bar} = 3.48$, TE polarization.

The FP resonance conditions for phases defined in Eq. (10) are simply

$$\psi_m = n\pi, \quad \text{where } n = 0, 1, 2, \ldots. \tag{11}$$

To further illustrate the concept of a supermode, we show an example of a 2×2 $\boldsymbol{\rho\varphi}$ matrix ($\lambda/\Lambda = 2.00391$, $t_g/\Lambda = 0.7162$, $\eta = 0.6$, $n_{bar} = 3.48$, TE polarization). The original $\boldsymbol{\rho\varphi}$ is undiagonal, indicating that the two waveguide array modes (TE$_0$, TE$_2$) are not orthogonal and would interact with each other at the HCG input/output planes. The diagonalization of the $\boldsymbol{\rho\varphi}$ matrix provides the eigenvector matrix $\mathbf{V}$, which can be used to orthogonalize the two waveguide array modes. The orthogonal modes set are termed "supermodes." The diagonal elements in the new $\boldsymbol{\rho\varphi}$ matrix describe how the supermodes propagate inside the HCG and reflect at the input/output plane. For this particular example, $\psi_2 = 0\pi$, indicating a FP resonance condition for the second-order supermode:

$$\boldsymbol{\rho\varphi} = \begin{bmatrix} 0.5534e^{-i0.2042\pi} & 0.1855e^{-i0.0569\pi} \\ 0.4743e^{i0.3554\pi} & 0.8757e^{-i0.0193\pi} \end{bmatrix},$$

$$\mathbf{V}^{-1}(\boldsymbol{\rho\varphi})\mathbf{V} = \begin{bmatrix} 0.4988e^{-i0.2798\pi} & 0 \\ 0 & 0.9993e^{i0.0000\pi} \end{bmatrix}.$$

Next, the analytical solutions of Eq. (11) are plotted on top of the reflectivity contour plots for comparison, shown as the white solid curves in Fig. 6(b). Two families of curves are seen. The nearly linear ones correspond to the zeroth-order supermode (more TE$_0$-like), $\psi_0 = n\pi$,

whereas the parabolic ones correspond to the second-order supermode (more TE_2-like), $\psi_2 = n\pi$. Excellent agreement is obtained between the analytical FP resonance lines and the reflectivity contour, testifying to the fact that the physics of the HCG features resides in Eq. (11).

The resonance curves originate from the $\omega-\beta$ diagram of TE_0 and TE_2 modes in Fig. 4. If the $\boldsymbol{\rho}$ matrix were diagonal and its elements real numbers, then the resonance curves would be totally determined by the $\omega-\beta$ diagram of the waveguide array modes. However, the $\boldsymbol{\rho}$ matrix is neither diagonal nor real. Indeed, it alters the resonance curves, and creates interesting phenomena at the intersection of the resonance curves; these intersection points corresponds to

$$|\Delta\psi| = |\psi_2 - \psi_0| = l\pi, \quad \text{where } l = 0, 1, 2, \dots. \qquad (12)$$

The intersection of the two resonance lines indicates that both modes reach their FP conditions *simultaneously*. For odd l, the two FP lines have an odd-number multiple of the π-phase difference, and the resonance lines simply cross each other, herein referred to as "crossing." On the other hand, for even l, the intersecting FP lines are in phase, and the two FP lines repel each other, forming an "anticrossing." The detailed views of these intersections are shown in the two right insets of Fig. 6(b). The crossing and anticrossing points typically represent high-Q resonance. We present further discussion of this topic in the following subsections.

For the TM-polarized light, the reflectivity contour is plotted in Fig. 7. There are several major differences from that of the TE case in Fig. 6. First, for this specific case of $\eta = 0.6$, both λ_{c2} and λ_{c4} are larger than those in the TE case, and there is a larger dual-mode region for broadband reflection. This, however, is not always the case for other η. Second, the resonance curves of the zeroth-order supermode are not as linear as those for the TE HCG. Third, there is a large range in the contour plot where the two supermode resonance curves are nearly overlaid on each other. All these originate from the difference between the $\omega-\beta$ diagrams of TE and TM waveguides, as shown in Fig. 4. Most notably, the slope of the $\omega-\beta$ curve of a TM waveguide is significantly different from that of a TE waveguide near the air light line region. This affects the $\boldsymbol{\varphi}$ matrix and thus the supermode resonance curves in Fig. 7.

In the following subsections, the mechanism of high reflectivity and 100% reflectivity, 100% transmission, and the high-Q resonance at the crossing and anticrossing points will be examined.

2.3a. Mechanism of High Reflectivity and 100% Reflectivity

As mentioned above, the HCG is inherently a two-mode device. Intuitively, if the two modes have complete destructive interference at the HCG output plane, the transmission will vanish, yielding a 100% reflectivity. Mathematically, this requires $\mathbf{T}_{00} = 0$, and thus $\tau_0 = 0$. According to Eq. (5a), $\boldsymbol{\tau} = \mathbf{E}(\boldsymbol{a} + \boldsymbol{b})$, and therefore we can summarize the 100% reflectivity condition as follows:

$$|\mathbf{R}_{00}| = 100\% \longleftrightarrow \tau_0 = [\mathbf{E}(\boldsymbol{a}+\boldsymbol{b})]_0 = \sum_m \mathbf{E}_{0m}(a_m + b_m) = 0. \qquad (13)$$
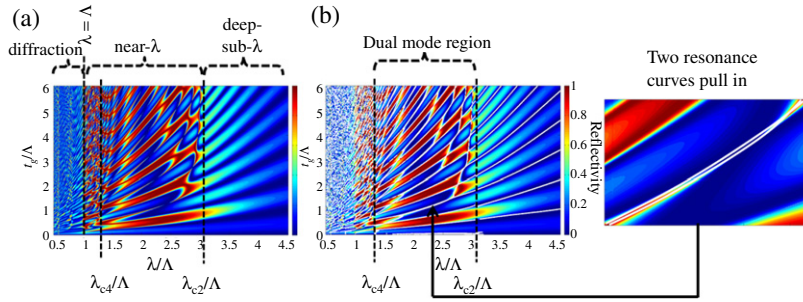
(a) Reflectivity contour of an HCG as a function of wavelength and grating thickness. The incident wave has a TM-polarized, surface-normal incidence. The mode cutoffs (λ_{c2}, λ_{c4}) and the first-order diffraction cutoff line $\lambda = \Lambda$ are marked to clearly illustrate the differences of the three wavelength-regimes: deep-subwavelength, near-wavelength, and diffraction. (b) Analytical solutions of FP resonance conditions of the individual modes [Eq. (11)], shown by the white curves, superimposed on the reflectivity contour in (a). Excellent agreement is obtained between the analytic solutions and the simulation results. The inset (right) shows that at some regions, the two resonance curves pull in together. HCG parameters are $\eta = 0.6$, $n_{\text{bar}} = 3.48$, TM polarization.

With Eqs. (5a), (1b) and (1d), τ_0 can be rewritten as follows (for TM light):

$$\tau_0 = \sum_m \mathbf{E}_{0m} (a_m + b_m)$$

$$= \left(\sqrt{\frac{\mu_0}{\varepsilon_0}} \gamma_0 / k_0 \right)^{-2} \sum_m (a_m + b_m) \Lambda^{-1} \int_0^\Lambda \mathcal{E}_{x,m}^{\text{II}}(x) \mathcal{E}_{x,0}^{\text{III}}(x) dx$$

$$= \left(\sqrt{\frac{\mu_0}{\varepsilon_0}} \gamma_0 / k_0 \right)^{-1} \sum_m (a_m + b_m) \Lambda^{-1} \int_0^\Lambda \mathcal{E}_{x,m}^{\text{II}}(x) dx = 0. \qquad (14)$$

The underlying concept in Eq. (14) is straightforward. At the HCG output plane, the overlap integral of the grating modes in region II with the zeroth-order transmissive plane wave $\mathcal{E}_{x,0}^{\text{III}}(x)$ indicates the total energy transferred from HCG to the zeroth-order transmissive plane wave. Since $\mathcal{E}_{x,0}^{\text{III}}(x)$ has a constant phase front along the x direction, the overlap integral reduces itself to the lateral average of all the grating modes at the HCG output plane. More generally, if we represent the overall field profile (from all grating modes combined) at the output plane just inside the grating, $z = t_g^-$, in terms of a Fourier series as a function of x (Λ being the Fourier series periodicity), the lateral average will merely have the mathematical meaning of the zeroth Fourier coefficient (DC coefficient). In general, the nth Fourier coefficient in such an expansion would correspond directly to the transmission coefficient τ_n of the $\pm n$th transmissive diffraction orders. However, since only the zeroth order carries power along z because of the subwavelength nature of HCG, it is only the DC Fourier coefficient that we need to suppress in order to have full reflection.

By applying the two-mode approximation, we obtain the simplified condition for 100% reflectivity:

$|\mathbf{R}_{00}| = 100\% \leftrightarrow$

$$\underbrace{(a_0 + b_0)\Lambda^{-1}\int_0^\Lambda \mathcal{E}_{x,0}^{\mathrm{II}}(x)dx}_{\substack{\text{lateral average of the 0th-order mode} \\ \text{(forward + backward) at } z = t_g^-}} \quad + \quad \underbrace{(a_2 + b_2)\Lambda^{-1}\int_0^\Lambda \mathcal{E}_{x,2}^{\mathrm{II}}(x)dx}_{\substack{\text{lateral average of the 2nd-order mode} \\ \text{(forward + backward) at } z = t_g^-}}$$

$$\underbrace{\phantom{(a_0+b_0)\Lambda^{-1}\int_0^\Lambda\mathcal{E}\qquad\qquad\qquad\qquad\qquad\qquad(a_2+b_2)\Lambda^{-1}}}_{\text{``destructive interference'' (cancellation) between the 0th-order and the 2nd-order modes at } z=t_g^-}$$

$$= 0. \tag{15}$$

We refer to the above two-mode-cancellation condition as the "destructive interference" between the two modes. We use quote marks because of the unusual *lateral-average* interpretation of interference. Figure 8 illustrates the destructive interference concept for a TE HCG. The average lateral electric fields of the two modes, i.e., $|(a_0 + b_0)\Lambda^{-1}\int_0^\Lambda \mathcal{E}_{y,0}^{\mathrm{II}}(x)dx|$ and $|(a_2 + b_2)\Lambda^{-1}\int_0^\Lambda \mathcal{E}_{y,2}^{\mathrm{II}}(x)dx|$, respectively, are plotted as a function of wavelength along with their phase difference $\Delta\phi = \text{phase}[(a_0 + b_0)\Lambda^{-1}\int_0^\Lambda \mathcal{E}_{y,0}^{\mathrm{II}}(x)dx] - \text{phase}[(a_2 + b_2)\Lambda^{-1}\int_0^\Lambda \mathcal{E}_{y,2}^{\mathrm{II}}(x)dx]$.

At the wavelengths of 100% reflectivity, the modes have equal intensities and opposite phase ($\Delta\phi = \pi$), i.e., a perfect cancellation [Eq. (15)], shown in Fig. 8(a). If two such 100% reflectivity points are located at close spectral vicinity, a broad band of high reflectivity is achieved.

Figure 8(b) illustrates the nontraditional DC-component interpretation for destructive interference. The lateral field profiles of zeroth- and second-order modes, $(a_0 + b_0)\mathcal{E}_{y,0}^{\mathrm{II}}(x, z = t_g^-)$ and $(a_2 + b_2)\mathcal{E}_{y,2}^{\mathrm{II}}(x, z = t_g^-)$ respectively, and the sum are plotted as a function of x. The summation field profile is zero **only** in terms of the DC-component. Had the grating not been subwavelength, this cancellation would not be enough to yield 100% reflection, since higher diffraction orders would not be zero and thus could transmit energy.

To further testify to this destructive interference concept, at the HCG output plane, the two modes' "magnitude difference" (defined as $|(a_0 + b_0)\Lambda^{-1}\int_0^\Lambda \mathcal{E}_{x,0}^{\mathrm{II}}(x)dx| - |(a_2 + b_2)\Lambda^{-1}\int_0^\Lambda \mathcal{E}_{x,2}^{\mathrm{II}}(x)dx|$ for TM polarization; for TE polarization, $\mathcal{E}_{x,m}^{\mathrm{II}}$ should be changed to $\mathcal{E}_{y,m}^{\mathrm{II}}$; the same applies to the definition of "phase difference") as well as "phase difference" (defined as $\Delta\phi = \text{phase}[(a_0 + b_0)\Lambda^{-1}\int_0^\Lambda \mathcal{E}_{x,0}^{\mathrm{II}}(x)dx] - \text{phase}[(a_2 + b_2)\Lambda^{-1}\int_0^\Lambda \mathcal{E}_{x,2}^{\mathrm{II}}(x)dx]$) are plotted against normalized wavelength and grating thickness (both by Λ), compared with the reflectivity contour plot, in Fig. 9. It is clearly seen that the checkerboard pattern aligns well with the two modes' phase difference contour. The amplitude difference, on the other hand, is relatively uniform. At the two modes' region, except at the resonance lines where the input plane wave is strongly coupled into one of the modes, the plane wave couples relatively uniformed to the two modes. Thus the two modes' phase difference dominantly determines the reflectivity contour. Furthermore, the HCG conditions that satisfy Eq. (15) are overlaid onto the reflectivity contour plot. Those

Figure 8
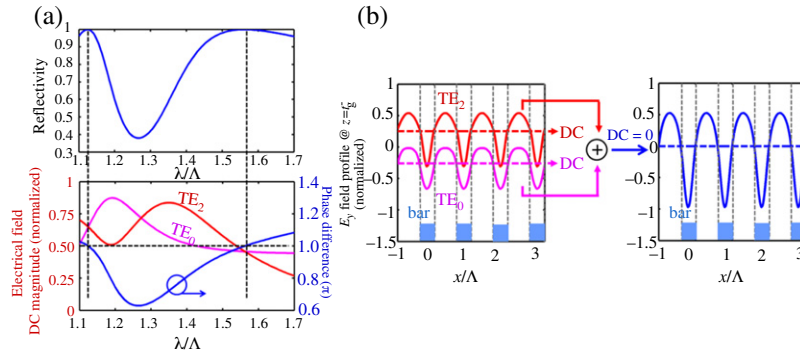
(a) Two-mode solution exhibiting perfect cancellation at the HCG output plane ($z = t_g^-$) leading to 100% reflectivity for TE-polarized light. At the wavelengths of 100% reflectivity (marked by the two vertical dashed lines), both modes have the same magnitude of the "DC" lateral Fourier component ($|(a_0 + b_0)\Lambda^{-1} \int_0^\Lambda \mathcal{E}_{y,0}^{II}(x)dx| = |(a_2 + b_2)\Lambda^{-1} \int_0^\Lambda \mathcal{E}_{y,2}^{II}(x)dx|$), but opposite phases: $\Delta\phi = \text{phase}[(a_0+b_0)\Lambda^{-1}\int_0^\Lambda \mathcal{E}_{y,0}^{II}(x)dx] - \text{phase}[(a_2+b_2)\Lambda^{-1}\int_0^\Lambda \mathcal{E}_{y,2}^{II}(x)dx] = \pi$. This means that the overall DC Fourier component is zero, which leads to the cancellation of the zeroth transmissive diffraction order. When two perfect-cancellation points are located in close spectral vicinity of each other, a broad band of high reflectivity is achieved. HCG parameters are $n_{bar} = 3.48$, $s/\Lambda = 0.4$, $t_g/\Lambda = 0.2$, and TE polarization of incidence. (b) Two-mode solution for the field profile at the HCG output plane ($z = t_g^-$) in the case of perfect cancellation. The cancellation is shown to be only in terms of the DC Fourier component. The higher Fourier components do not need to be zero, since subwavelength gratings have no diffraction orders other than zeroth order. The left-hand plot shows the decomposition of the overall field profile into the two modes, whereby the DC components of these two modes cancel each other. HCG parameters are the same as (a), and $\lambda/\Lambda = 1.563$; this is the condition corresponding to the dashed line on the right-hand side in (a).

are exactly the high-reflectivity regions. Excellent agreement is thus achieved between the simulation results and the physical insights given by Eq. (15). If one plots a series of contour plots with different duty cycles η, one can easily choose an η and a t_g to design a broadband high-reflection mirror.
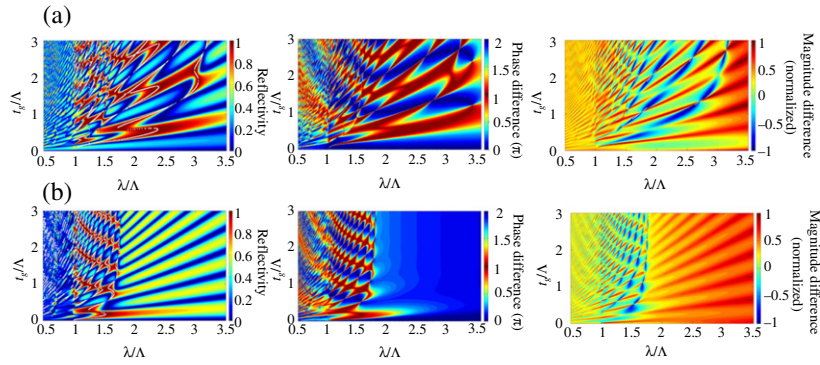
2.3b. Mechanism of 100% Transmission

Similar to the analysis for the 100% reflection, the 100% transmission in the two-mode region can also be explained by the interference concept. With Eqs. (1a) and (1b) for the input, Eq. (1d) for the output, and Eq. (5a), we get the following condition for 100% transmission:

$$|\mathbf{T}_{00}| = 100\% \longleftrightarrow |\tau_0| = |[\mathbf{E}(a+b)]_0| = \left|\sum_m \mathbf{E}_{0m}(a_m + b_m)\right| = 1. \quad (16)$$

Figure 9

(a)

(b)

Reflectivity contour plot compared with the two modes' "phase difference" at the HCG output plane (defined as $\Delta\phi = \text{phase}[(a_0 + b_0)\Lambda^{-1}\int_0^\Lambda \mathcal{E}_{x,0}^{II}(x)dx] - \text{phase}[(a_2 + b_2)\Lambda^{-1}\int_0^\Lambda \mathcal{E}_{x,2}^{II}(x)dx])$ and "magnitude difference" at the HCG output plane (defined as $|(a_0 + b_0)\Lambda^{-1}\int_0^\Lambda \mathcal{E}_{x,0}^{II}(x)dx| - |(a_2 + b_2)\Lambda^{-1}\int_0^\Lambda \mathcal{E}_{x,2}^{II}(x)dx|$ for TM polarization; for TE polarization, $\mathcal{E}_{x,m}^{II}$ should be changed to $\mathcal{E}_{y,m}^{II}$; the same applies to the definition of "magnitude difference"). The white curves overlaid onto the reflectivity contour plot indicate the HCG conditions where Eq. (15) is satisfied. At the two-modes region, except at the resonance curves, the input plane wave couples relatively equal to both modes. Thus their phase difference dominantly determines the reflectivity. (a) TM HCG, $\eta = 0.75$, $n_{\text{bar}} = 3.48$. (b) TE HCG, $\eta = 0.45$, $n_{\text{bar}} = 3.48$.

As for Eq. (14), τ_0 can be rewritten as follows (for TM light):

$$
\begin{aligned}
|\tau_0| &= \left| \sum_m \mathbf{E}_{0m}(a_m + b_m) \right| \\
&= \left| \left(\sqrt{\frac{\mu_0}{\varepsilon_0}} \gamma_0/k_0 \right)^{-2} \sum_m (a_m + b_m)\Lambda^{-1}\int_0^\Lambda \mathcal{E}_{x,m}^{II}(x)\mathcal{E}_{x,0}^{III}(x)dx \right| \\
&= \left| \left(\sqrt{\frac{\mu_0}{\varepsilon_0}} \gamma_0/k_0 \right)^{-1} \sum_m (a_m + b_m)\Lambda^{-1}\int_0^\Lambda \mathcal{E}_{x,m}^{II}(x)dx \right| = 1. \quad (17)
\end{aligned}
$$

Equation (17) further implies that

$$
\left| \sum_m (a_m + b_m)\Lambda^{-1}\int_0^\Lambda \mathcal{E}_{x,m}^{II}(x)\,dx \right| = \sqrt{\frac{\mu_0}{\varepsilon_0}}. \quad (18)
$$

The underlying concept in Eq. (18) is that at the HCG output plane the lateral average of all the grating modes (magnitude) equals the lateral field average of the input plane wave. In other words, the DC Fourier component of the grating modes in the HCG output plane has the same magnitude as the input plane wave in region I. When these grating modes outcouple to the zeroth-order plane wave in region III, it has the same magnitude as the input plane wave, and thus 100% transmission happens. Furthermore, at the HCG input plane, the DC

Figure 10
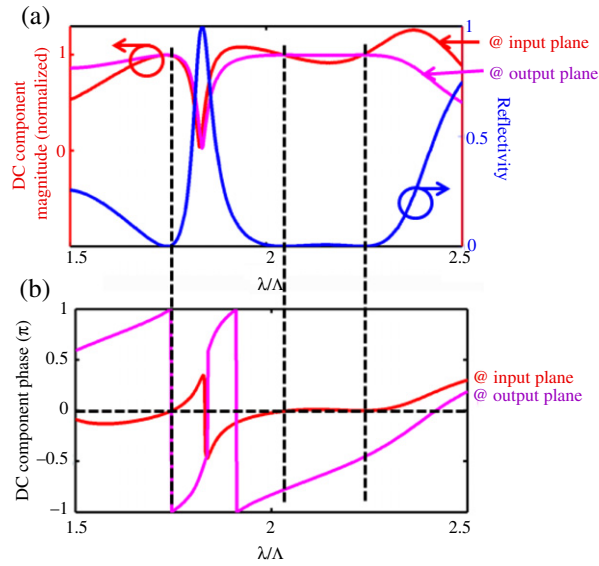
Magnitude (a) and phase (b) spectrum of the two grating modes' lateral average $\sum_{m=0,\,2} (a_m + b_m) \Lambda^{-1} \int_0^\Lambda \mathcal{E}_{x,m}^{II}(x)\,dx$ at the HCG output plane, and $\sum_{m=0,2} \left[a_m e^{+j\beta_m t_g} + b_m e^{-j\beta_m t_g} \right] \Lambda^{-1} \int_0^\Lambda \mathcal{E}_{x,m}^{II}(x)\,dx$ at the input plane, compared with the reflection spectrum. At the 0% reflection points (i.e., 100% transmission points), marked by the three vertical dashed lines, Eqs. (18) and (19) are satisfied. The input light is TM-polarized, HCG $t_g/\Lambda = 0.84$, $\eta = 0.55$, $n_{\text{bar}} = 3.48$.

Fourier component of the grating modes should also equal that of the input plane wave, so that the input plane wave can fully couple into the grating. This implies

$$\sum_m \left[a_m e^{+j\beta_m t_g} + b_m e^{-j\beta_m t_g} \right] \Lambda^{-1} \int_0^\Lambda \mathcal{E}_{x,m}^{II}(x)\,dx = \sqrt{\frac{\mu_0}{\varepsilon_0}}. \tag{19}$$

Note that the left side of Eq. (19) does not contain a modulus sign, meaning that not only the magnitude but also the phase should match. This results from the fact that in order to cancel any reflection at the input plane, the impedance has to be completely matched, not only magnitude, but also phase. At the HCG output plane, the phase of $\sum_m (a_m + b_m) \Lambda^{-1} \int_0^\Lambda \mathcal{E}_{x,m}^{II}(x)\,dx$ determines the phase of the output plane wave. To testify this concept, at the two-mode region, we plot the magnitude and phase spectrum of the two grating modes' lateral average $\sum_{m=0,2} (a_m + b_m) \Lambda^{-1} \int_0^\Lambda \mathcal{E}_{x,m}^{II}(x)\,dx$ at the HCG output plane, and $\sum_{m=0,2} \left[a_m e^{+j\beta_m t_g} + b_m e^{-j\beta_m t_g} \right] \Lambda^{-1} \int_0^\Lambda \mathcal{E}_{x,m}^{II}(x)\,dx$ at the input plane, shown in Fig. 10. It is clearly seen that at 0% reflectivity points (i.e., 100% transmission points), the two grating modes' lateral average matches the input plane wave at the HCG input plane, for both the magnitude and phase; whereas at the HCG output plane, its magnitude is the same as that of the input plane wave, indicating 100% transmission.
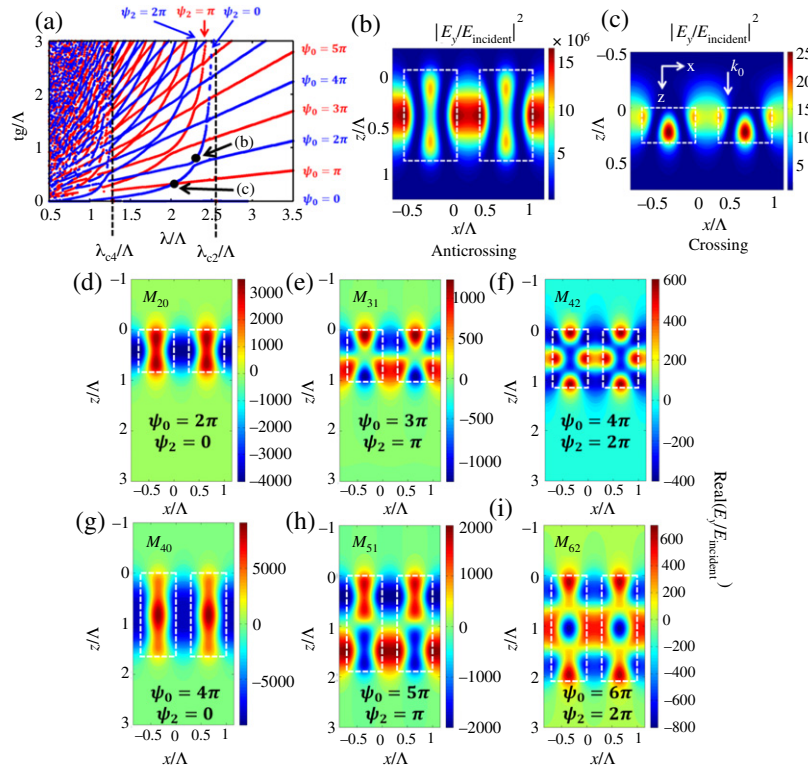
2.3c. Crossings and Anticrossings

The phenomena of band anticrossings are commonly observed in physics and, more specifically, optics. Examples include coupled quantum-dot cavities [50,51], semiconductor alloys [52], photonic crystals [53], optical modulators [54], and many others. In all cases, anticrossings are known to be indicators of strong coupling, while crossings typically indicate weak or no coupling.

Figure 6 shows the crossing and anticrossing phenomena in the HCG reflectivity contour plot (t_g–λ diagram). Within optics and electromagnetism, crossings and anticrossings are typically presented in ω–β diagrams, rather than in a t_g–λ diagram, which we chose because the effect can be more clearly seen. However, the two representations are indeed very similar, since as we mentioned above, $\psi_m = n\pi$ is merely a generalization of the simpler condition $t_g = n\pi\beta_m^{-1}$, and therefore the resonance curves in Fig. 6 are equivalent to a β^{-1}–ω^{-1} diagram. Hence, all intuitions behind crossings and anticrossings in standard texts apply.

Figure 11(a) shows the resonance curves in the t_g–λ diagram. It is clearly seen that when two resonance curves intersect each other, anticrossing happens if $|\triangle\psi| = |\psi_0 - \psi_2| = 2l\pi$; whereas crossing happens if $|\triangle\psi| = |\psi_0 - \psi_2| = (2l + 1)\pi$. We expect high-Q resonance phenomenon around the anticrossing points: when the two intersecting resonance lines are in phase, the FP resonances have the same *parity* (both odd, or both even), and their intensity profiles overlap significantly, which leads to strong coupling between them and results in an anticrossing. In contrast, an opposite parity between the two resonances leads to a weak coupling, resulting in a crossing.

Figures 11(b) and 11(c) present the intensity profiles in the grating for the cases of an anticrossing and a crossing, respectively. Anticrossing corresponds to a very strong resonance, where a very significant (10^7-fold) intensity buildup occurs within the grating. On the other hand, crossing is shown to correspond to a fairly weak ($25\times$) energy buildup. Figures 11(d)–11(i) show the field profile of the anticrossing conditions. We relate the resonance orders to how many times the electrical field envelope crosses zero or how many times it reaches peak values (positive or negative) along the z axis in the middle of the HCG bar or air gap [nth order, electrical field envelope crosses zero $n - 1$ times and reaches peak value (positive or negative) n times in general]. All anticrossings that are located along the rightmost parabolic resonance line (corresponding to $\psi_2 = 0$) yield first-order resonances, where the electrical field envelope does not cross zero; all anticrossings that are located along the second rightmost parabolic resonance line ($\psi_2 = \pi$) yield second-order resonances, where the electrical field envelope crosses zero once. In other words, the resonance order is determined by ψ_2. Herein, we assign two indices based on ψ_0 and ψ_2 for each resonance, such as M_{20} (intersection of $\psi_0 = 2\pi$ and $\psi_2 = 0\pi$), M_{24} (intersection of $\psi_0 = 2\pi$ and $\psi_2 = 4\pi$), etc. See examples in Figs. 11(d)–11(i).

Figure 11

(a) Resonance lines on t_g–λ diagram. Depending on $|\triangle\psi|$, the intersecting resonance curves either crosses or anticrosses. HCG parameters: $\eta = 0.70$, $n_{bar} = 3.48$, TE polarization light. (b) Intensity profile inside the grating for an anticrossing, showing 10^7-fold resonant energy buildup. The input light is TE polarized, $\lambda/\Lambda = 2.32912867$, HCG $t_g/\Lambda = 0.8415$, $\eta = 0.70$, $n_{bar} = 3.48$. (c) Intensity profile for a crossing, showing only weak energy buildup. The input light is TE polarized, $\lambda/\Lambda = 2.02$, HCG $t_g/\Lambda = 0.32$, $\eta = 0.70$, $n_{bar} = 3.48$. The HCG conditions for (b) and (c) are labeled in the t_g–λ diagram in (a). (d)–(i) Field profile [real($E_y/E_{incident}$)] of different orders of HCG resonance at anticrossings: (d), (g) first order; (e), (h) second order; (f), (i) third order. The assigned index for each resonance is labeled in the figures. The HCG parameters for (d)–(i) are $\lambda/\Lambda = 2.32912867$, $t_g/\Lambda = 0.8415$; $\lambda/\Lambda = 2.04704662$; $t_g/\Lambda = 1.0267$; $\lambda/\Lambda = 1.80528405$, $t_g/\Lambda = 1.1555$; $\lambda/\Lambda = 2.32912867$, $t_g/\Lambda = 2.452394271$; $\lambda/\Lambda = 2.313806663$, $t_g/\Lambda = 1.8975$; $\lambda/\Lambda = 2.164125301$, $t_g/\Lambda = 2.0857$. For all conditions, the input light is TE polarized, HCG $\eta = 0.70$, $n_{bar} = 3.48$. [Note that (b) and (d) are the same HCG resonance.]

2.3d. Resonance Mechanism of High-Contrast Gratings

As seen from the above discussion, the resonance curves shown in Figs. 6 and 11 represent the HCG resonance. The HCG resonance mechanism is greatly different from a plain simple FP cavity. In a plain simple FP cavity, the FP modes represent *orthogonal* modes of a cavity, which do not couple into each other at the exiting planes (reflectors). The uniquely interesting case of the HCG resonator is that the propagating waveguide

array modes inside the grating actually *strongly couple into each other* at the input/output planes due to the *abrupt change in the spatial distribution of refractive index*. This makes the FP analysis a matrix one rather than scalar. We will have a more insightful and quantitative discussion on the mechanism of HCG resonance in this section.

The HCG resonance occurs when the supermode, an ensemble of the orthogonal waveguide array modes, is self-sustainable. By finding the eigenvector of the $\boldsymbol{\rho\phi}$ matrix, one can find a new basis of mode sets for the HCG, which are orthogonal to each other. These new mode sets are termed "supermodes," as discussed in the previous sections. A self-sustainable supermode **C** satisfies the round-trip condition $\mathbf{C} = \boldsymbol{\rho\phi\rho\phi}\mathbf{C}$, or equivalently, $(\mathbf{I} - \boldsymbol{\rho\phi\rho\phi})\mathbf{C} = \mathbf{0}$, **I** being a unit matrix. Clearly, for a nonzero solution to exist on such an equation, the following condition must be satisfied:

$$\det[\mathbf{I} - (\boldsymbol{\rho\phi})^2] = 0. \tag{20}$$

Equation (20) is the HCG resonance condition. The ability to reduce the elaborate nature of HCGs into a single half-round-trip matrix $\boldsymbol{\rho\phi}$ is a significant advantage of Eq. (20). When this requirement is satisfied, the boundary conditions at both HCG input and output planes are satisfied solely by the internal supermode, leaving no need for outside excitation. This description is simply a matrix-form paraphrase of the already well-known round-trip description of a regular FP resonance.

There are two major advantages of using an HCG resonator over a traditional FP resonator. First, the entire cavity can be ultrathin, much less than a half-wavelength. Second, the HCG waveguide array modes couple into each other upon reflection from the HCG input and output planes. This coupling allows a completely excellent optical resonator without traditional high-reflectivity mirrors!

Equation (20) can predict the HCG resonant wavelengths. To verify this, we plot in Fig. 12(a) an HCG reflectivity spectrum containing five resonances, calculated by RCWA. The first among the five resonances has a very narrow linewidth with an approximate Q factor of $\sim 10^9$, while the additional resonances are broader. Also in Fig. 12(a) are the absolute values of $\det[\mathbf{I} - (\boldsymbol{\rho\phi})^2]$, showing that, indeed, minima of $|\det[\mathbf{I} - (\boldsymbol{\rho\phi})^2]|$ predict the exact wavelengths of all five resonances, and the narrowest of the five resonances corresponds to $|\det[\mathbf{I} - (\boldsymbol{\rho\phi})^2]|$ falling closest to zero.

While Eq. (20) describes an idealized ("infinite" Q) resonance, for finite HCG quality factors, a more general expression is needed. When a constant excitation is stimulated by an incident plane wave, several supermodes would be excited. Energy will gradually start building up within each supermode, according to its own Q_j. The supermode with the highest Q_j will build up energy faster than the rest, and will eventually dominate. Thus we can argue that the highest Q_j can represent the Q value of the entire structure.

The Q_j value of each HCG supermode can be expressed as

$$Q_j = 2\pi t_g \left(n_{gr}/\lambda\right) \left|r_j / \left(1 - r_j^2\right)\right|. \tag{21}$$
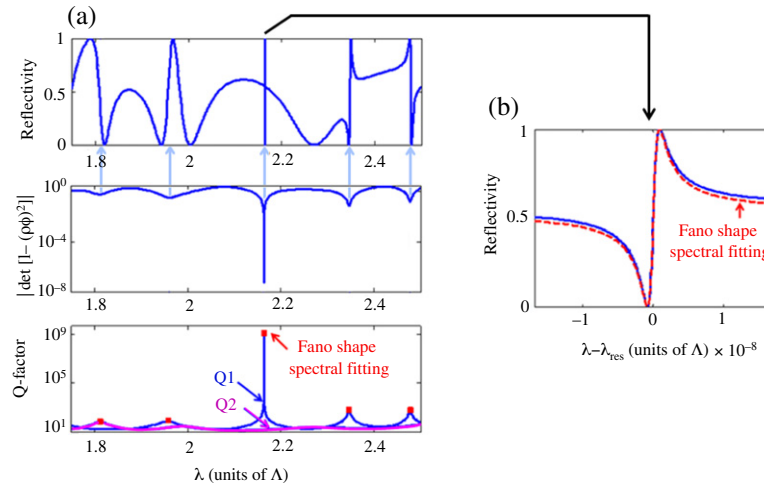
(a) Validation of the HCG resonance condition $\det[\mathbf{I} - (\boldsymbol{\rho}\boldsymbol{\varphi})^2] = 0$. The absolute value of the determinant in Eq. (20) is plotted against the reflectivity spectrum of the HCG, containing five resonances (one strong and four weaker). The figure shows that not only do the dips of the determinant predict the exact resonant wavelengths, but also the closer the determinant to zero, the stronger the resonance. The bottom plot validates the HCG Q factor formulation in Eqs. (21) and (22). The overall Q factor of the HCG is the maximal among Q_j. The spikes of Q are shown to predict precisely the wavelengths of the resonances in the reflectivity spectrum. The Q factor is in good agreement with a known method of inferring Q factors by curve fitting to Fano-resonant line shapes [55]. (b) Example of Fano-shape spectral fitting. The HCG parameter is $\eta = 0.7$, $t_g/\Lambda = 2.086$, and $n_{\mathrm{bar}} = 3.48$. The polarization of the incident light is TE [45].

The supermodes are eigensolutions of the HCG, and therefore r_j in Eq. (21) is the jth eigenvalue of the half-round-trip matrix $\boldsymbol{\rho}\boldsymbol{\varphi}$. n_{gr} is the effective group index of the FP cavity.

The overall HCG Q factor is the *maximal* among the Q_j in Eq. (21):

$$Q_{\mathrm{HCG}} = \max Q_j. \tag{22}$$

The Q-factor formalism described in Eqs. (21) and (22) can be verified against a known method for Q-factor extraction by spectral curve fitting to Fano resonance line shapes [55] . [Figure 12(b) shows an example.] The agreement between the two methods is excellent, as is evident from Fig. 12(a), which presents the two highest Q_j from Eq. (21), the maximal of which is the overall HCG Q factor. As expected, Q_{HCG} exhibits peaks at the exact wavelengths at which the five resonances are located, and the values of Q are in agreement with the spectral sharpness of the resonances. It is important to emphasize that while both our method and the Fano-resonance method are in very good agreement, our calculation does not rely on curve fitting. Rather, we calculate the Q factor directly from the HCG geometry. Note this design is optimized to reach a Q value as high as 10^9.

3. High-Contrast-Grating-Based Vertical-Cavity Surface-Emitting Lasers

The surface-emitting laser was first proposed by K. Iga [56]. Significant advance was made possible only after epitaxy technology became mature enough for precision growth of many pairs of DBRs [57–59]. These renditions of surface-emitting lasers, with active region sandwiched between two highly reflecting DBRs, are referred to as vertical-cavity surface-emitting lasers (VCSELs). The DBRs typically consist of layers of materials with alternating high and low refractive indices. The first planar VCSEL structure using proton implantation was proposed and demonstrated, which facilitated fabrication of large VCSEL arrays and multiwavelength arrays [60,61]. It was shown that multiple transverse mode VCSELs can be obtained with a large aperture [62] and directly modulated at multiple gigabit per second rates. The use of a multiple transverse mode VCSEL as a transmitter through low-cost multimode fiber for high-speed optical interconnect applications was first suggested and demonstrated in 1991 [63]. Transmitters were developed in the mid-1990s and have been dominating the transceiver market for gigabit per second local area networks (LANs) [63,64]. Currently, the majority of lasers manufactured are 850 nm VCSELs. Most of them are directly modulated, multiple transverse mode VCSELs for LAN applications and single-mode continuous-wave (CW)-operated VCSELs for optical mouse applications. In addition, VCSELs emitting in the 1300–1550 nm wavelength regime will be promising as low-cost laser sources for sensing and spectroscopy applications, high-speed optical interconnects in data centers, and next-generation access networks and passive optical networks (PONs) [65].

The VCSEL typically has a small round-trip gain, typically <1%, owing to the very short gain length, i.e., the total quantum well thickness. Hence, a very high total reflectivity (>99%) is required from the mirrors. The DBRs are typically very thick. For example, for an 850 nm wavelength VCSEL, a single DBR typically consists of more than 25 pairs of quarter-wavelength alternating index materials.

For 1300 or 1550 nm, because of the smaller index difference available in the InGaAlAs/InGaAsP/InP material system, the pair number needs to be more than doubled, making the epitaxial growth extremely challenging. In addition, owing to a much higher free-carrier absorption in p-doped DBRs, the VCSEL's top DBR is particularly difficult to implement. Typically the top mirror is formed by either evaporating a dielectric mirror [66,67], wafer fusing a DBR epitaxially grown on another material system [68], or metamorphically growing a GaAs/AlGaAs top DBR [69]. These options are technologically challenging from a growth and fabrication standpoint and relatively costly compared with using a monolithic structure already including a p-GaAs/AlGaAs DBR like those used in short-wavelength VCSELs. It suffices to say that the DBR remains the most challenging problem for the realization of VCSELs at various wavelengths.

The HCG can be easily incorporated into a VCSEL, totally replacing the top DBR. Electrically pumped HCG VCSELs have been demonstrated at wavelengths of 850, 980, and 1320 nm and recently 1550 nm. In

Figure 13
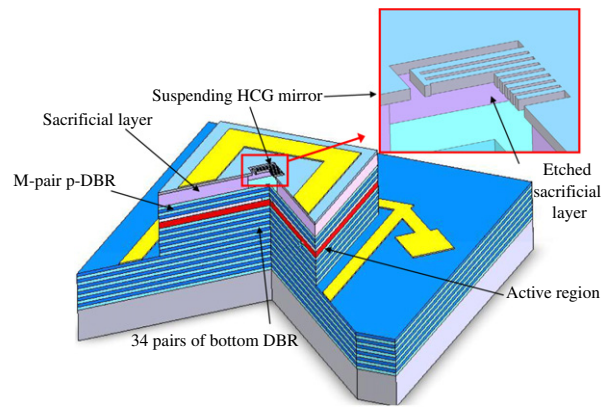
Schematic of a typical 850 nm design, consisting of an HCG-based top mirror, a 5/4-λ air gap, a λ-cavity containing an active region, and a conventional semiconductor-based bottom n-DBR mirror. Here $M = 2$ or 4 [14].

addition, widely tunable VCSELs are also reported. In the following, we summarize the design and realization of 850 and 1550 nm HCG VCSELs.

3.1. 850 nm Oxide-Confined Vertical-Cavity Surface-Emitting Lasers

Our group reported the first HCG incorporation into a VCSEL with an 850 nm oxide-confined VCSEL design [14], shown in Fig. 13. The structure consists of an HCG-based top mirror, a 5/4-λ air gap, a λ-cavity containing an active region, and a conventional semiconductor-based bottom n-DBR mirror. Electric current injection is conducted through the top metal contact via the p-doped HCG layer through the bottom metal contact. Current confinement is achieved through the use of an aluminum oxide aperture.

For 850 nm VCSELs, the typical HCG dimension for period (Λ), air gap (a), and thickness (t_g) are 380, 130, and 235 nm, respectively, for a TM HCG, and 620, 400, and 140 nm, respectively, for a TE HCG. The fabrication process of the HCG VCSEL includes (1) definition of the HCG by electron-beam lithography, (2) a wet or dry etching process to form the HCGs, (3) metallization, (4) oxidation for current confinement, and (5) selective etch process to remove a GaAs sacrificial material underneath the HCG layer, making the HCG a freely suspended structure.

Single-mode, CW operation of HCG VCSELs, was demonstrated for both TM HCG and TE HCG at room temperature. The device has very low, submilliampere threshold currents and output power >1 mW. Single-mode emission with a >40 dB side mode suppression ratio was obtained. A Gaussian fundamental mode near-field emission was obtained, which was determined by the VCSEL cavity despite the square shape of HCG, as depicted in Fig. 14. This is very similar to the modes observed in standard DBR-based VCSELs [62].
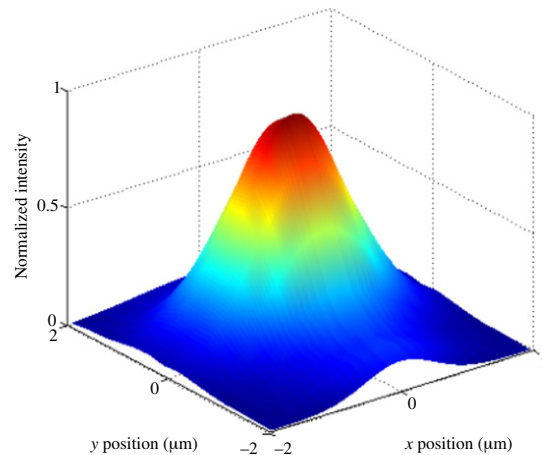
Typical near-field intensity distribution, showing a Gaussian fundamental mode determined by the VCSEL cavity, despite the square shape of the HCG [18].

In a conventional VCSEL, polarization modes are degenerate and randomly oriented. Lacking a determined polarization can cause mode partition noise in an optical communication link [65]. Many publications have been devoted to this problem [70–74]. The inherent reflectivity difference between TM- and TE-polarized light in an HCG, on the other hand, results in a large polarization-dependent modal loss. Thus, the HCG is ideal for lithographically defined polarization mode control. A typical polarization selection ratio >30 dB is obtained with HCG VCSELs.

3.2. 1550 nm Proton-Implanted Vertical-Cavity Surface-Emitting Lasers

Long-wavelength VCSELs are more challenging to realize than GaAs-based VCSELs because of several major technical challenges posed by the InP-based material system, the most difficult of which are high-reflectivity p-DBRs and the forming of current-confined apertures. Forming a current aperture in an InP-based system is challenging because there is no easily oxidizable material in the system. This problem has been overcome by forming a buried heterostructure in the VCSEL structure [66] or by etching away layers in the middle of the VCSEL structure [75]. Using pseudomorphic growth of GaAs-based materials above the active region, an oxide aperture can also be formed [69]. These approaches are technically difficult and add expense to mass manufacturing long-wavelength VCSELs. With the use of an HCG, there is a great reduction in epitaxial layer thickness above the active region. Hence, proton implantation can be used to form current apertures. This permits the use of only one epitaxy step and simple fabrication, a feature that is very promising for manufacturing high-yield, low-cost, long-wavelength VCSELs.

Figure 15
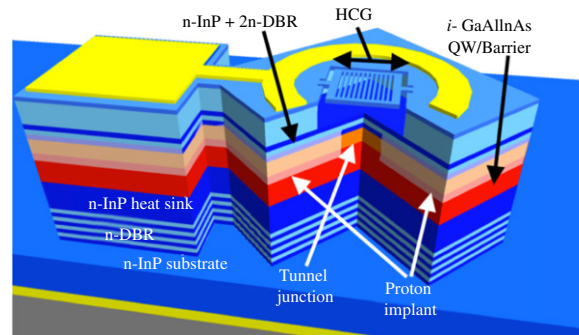
Schematic of a 1550 nm VCSEL with a suspended TE HCG in place of a typical top DBR. Current confinement is provided through the use of a proton-implant-defined aperture [19].

3.2a. Design and Fabrication

A cross section of the device is shown schematically in Fig. 15. It consists of, starting from the substrate side, 40–60 pairs of n-DBRs, an InP heat sink layer, an active region with GaAlInAs quantum wells, and a thin layer of p-GaAlInAs, followed by a tunnel junction. Above the tunnel junction there are two pairs of n-DBRs, followed by a ~1.8 μm air gap and a 195 nm thick InP HCG. The grating is $12 \times 12\ \mu m^2$ wide in all cases described here. Electrical confinement is provided in the structure by a proton implantation at a depth near the tunnel junction. The size of the proton implant aperture is varied from 8 to 25 μm. Contacts are deposited on the back side of the wafer and top side on a contact layer above the HCG layer and surrounding the etched HCG.

The HCG in this structure is an InP layer with a thickness of 195 nm, a period of 1070 nm, and a semiconductor grating bar width of 370 nm. The grating is designed to highly reflect light with its electric field polarized parallel to the direction of the grating bars (TE), but not to the orthogonal polarization (TM). The grating is optimized so that it has a wide tolerance in the air gap dimension for ease of fabrication. Device fabrication was carried out as follows. A current aperture was formed by protecting the aperture area by a thick photoresist, followed by a H^+ ion implantation. A top annular n-contact subsequently was fabricated by lithography, metal evaporation and liftoff. A mesa was etched around the contact ring to the depth of the n-DBRs to electrically isolate the devices from each other.

The HCG was defined by electron beam lithography and transferred by several steps of wet etching. In principle, the pattern could also be defined by using a standard deep ultraviolet lithography stepper. The HCG is then released by a selective etch of a sacrificial region below the HCG, followed by critical point drying to prevent the structure from being damaged during the drying process. A scanning electron microscope image of a completed HCG VCSEL is shown in Fig. 16(a). An enlarged scanning electron microscope image of the HCG is shown in Fig. 16(b).
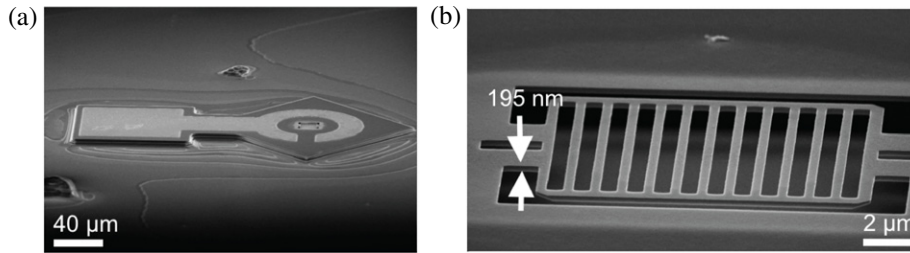
Scanning electron microscope images of (a) a completed 1550 nm HCG VCSEL. (b) Enlarged image of the HCG, which is just 195 nm thick [19].
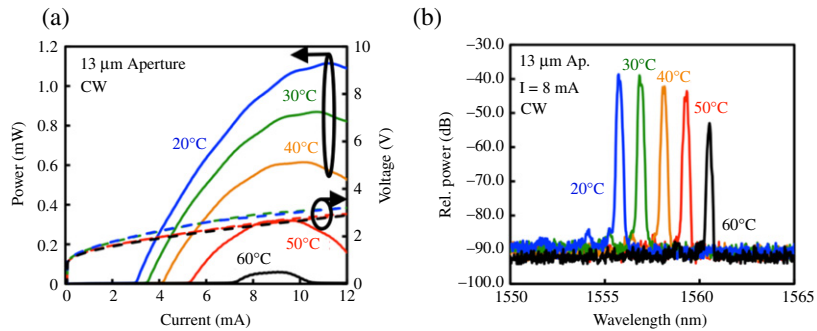
Light– (solid lines) and voltage–current (dashed lines) characteristics of an HCG VCSEL with a 13 μm proton implant aperture at various heat sink temperatures. Devices show over 1.1 mW output power at room temperature and operate CW to >60°C. (b) Spectrum of the same device under various heat sink temperatures. A wavelength shift of 0.12 nm/K is extracted [19].

3.2b. Optical and Modulation Characteristics

Excellent electrical and optical characteristics were obtained with VCSELs with various implant aperture sizes, ranging from 5 to 20 μm, and fixed HCG size of 12×12 μm^2. Figure 17(a) shows the light–current (solid) and voltage–current (dashed) characteristics of a VCSEL with a 13 μm proton implant aperture at various heat sink temperatures. This VCSEL has a threshold current of ~3 mA at room temperature and lases CW at temperatures exceeding 60°C. The room temperature peak output power is ~1.1 mW with slope efficiencies >0.25 mW/mA. Recently, with further optimization of epitaxial structures, CW operation up to 85°C and >3 mW CW output power at room temperature was achieved [26]. Furthermore, we demonstrated >7.5 GHz 3 dB direct modulation bandwidth [26].

Optical spectra for an HCG VCSEL, biased at a constant current of 8 mA, measured at various heat sink temperatures are shown in Fig. 17(b). Athermal resistance of 1.55 K/mW is obtained, indicating good heat transfer away from the active region. At all biases, the VCSELs emit in a single transverse mode with a side mode suppression
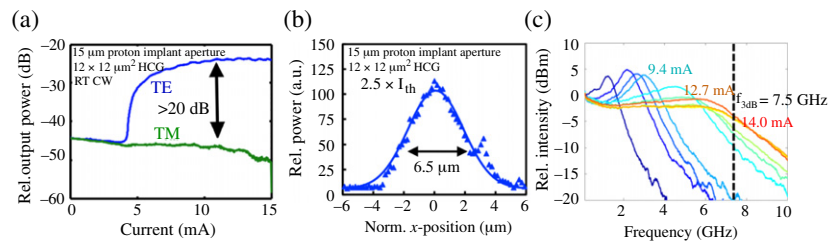
(a) Polarization-resolved light–current characteristics of a 1550 nm HCG VCSEL. A polarization suppression ratio of >20 dB is achieved, with the measurement limited by the polarizer [19]. (b) Near-field intensity profile of the device at $2.5 \times I_{th}$ (where I_{th} is threshold current). A FWHM of ~6.5 μm is obtained with a VCSEL with a proton implant aperture size of 15 μm [19]. (c) Frequency response (S21 characteristics) of a directly modulated 1550-nm HCG VCSEL under room temperature CW operation, biased at various current levels [26].

ratio >45 dB. HCG VCSELs are polarization stable because of the high differentiation between the reflectivity in the orthogonal electric field polarizations. Figure 18(a) shows the polarization-resolved light–current characteristics of a device with a 15 μm proton implant aperture and 12×12 μm² HCG. The orthogonal polarization is suppressed by >20 dB (limited by the polarizer in the experimental setup).

Since proton-implant-defined apertures provide little optical index guiding, it is possible to achieve larger size apertures while maintaining a single transverse mode emission profile. This makes the devices ideal for high coupling efficiency to a single-mode fiber. The near-field intensity profile of a device with a 15 μm proton implant aperture and 12 μm × 12 μm HCG is shown in Fig. 18(b). This device emits in a single fundamental transverse mode with a full width at half-maximum (FWHM) of ~6.5 μm. Generally, the devices have FWHMs of 40%–50% of their lithographically defined aperture size. VCSELs with >20 μm proton-implant-defined apertures show no significant higher-order transverse mode, since the finite area of HCG reflectivity (12 μm × 12 μm) contributes to the suppression of the higher-order transverse modes in the largest-aperture devices.

The HCG VCSEL was tested under direct modulation. The frequency response (S21 characteristics) of a fixed wavelength VCSEL are shown in Fig. 18(c) as a function of bias up to 14 mA [26]. The device has a −3 dB point of 7.5 GHz, which is currently limited by RC (resistor–capacitor) parasitics. Large signal modulation with an open eye at 10 Gbit/s is achieved. Currently, experiments in transmission through optical fibers are being conducted.

3.3. Tunable VCSELs

Tunable lasers are recognized as a highly desirable components for many applications, including spectroscopy, communications, and

sensing [76,77]. In particular, tunable 1550 nm lasers are important for wavelength-division-multiplexed (WDM) systems with applications including sparing, hot backup, and fixed-wavelength laser replacement for inventory reduction. They give network designers another degree of flexibility to drive down the overall system cost. Tunable VCSELs are desirable because of their simple, continuous tuning characteristics and low power consumption, making them promising for low-cost applications.

A wavelength-tunable VCSEL has been constructed by suspending its top DBR by a microelectromechanical structure (MEMS) [78–85]. The DBR is moved by a voltage across an air gap with the rest of the laser cavity, which tunes the emission wavelength over a large and continuous tuning range. Previous MEMS VCSELs had relatively large MEMS, typically ∼200 µm long and 10–20 µm wide, because the MEMS scaled with the DBR thickness [78]. This leads to a slow tuning speed and processing challenges. Using ultrathin HCGs, which are 10–20 times thinner than a typical DBR, the other two dimensions of the MEM structure can be reduced by similar numbers, resulting in a close to 3 order of magnitude increase in tuning speed. An ultrafast tunable 850 nm VCSEL was obtained with a 27 MHz mechanical tuning speed by using a 3 µm × 3 µm HCG consisting of merely four periods [17]. Another major consequence of using an ultrathin HCG is that a proton-implanted structure may be used also for tunable VCSELs [26]. This is particularly important for a 1550 nm VCSEL structure where native oxide is not readily available. Here we review the two structures and performance.

3.3a. Ultrafast Tunable Oxide-Confined VCSEL

The schematic of a tunable oxide-confined VCSEL is shown in Fig. 19. The device consists of an n-doped HCG top mirror, a sacrificial layer, two pairs of p-doped DBR, an AlGaAs oxidation layer, a cavity layer containing the active region, and a bottom standard n-doped DBR mirror, all monolithically grown on a GaAs substrate. Electrical current injection is conducted through the middle laser p-contact (via two pairs of p-doped DBRs above the cavity layer) and back side n-contact (via the substrate). An aluminum oxide aperture is formed on the AlGaAs layer just above the active region to provide current and optical confinement. The HCG is freely suspended above a variable air gap and supported via a nanomechanical structure. The tuning contact is fabricated on the top n-doped HCG layer. The top two contacts provide a bias across the gap between the HCG and the active region. With a reverse bias in this junction, the electric field resulting from the p–n junction charges attracts the HCG downward, which thus shortens the laser cavity length and blueshifts the lasing wavelength.

A typical tunable oxide-confined VCSEL with TM HCG has a very low threshold current of 200 µA and an external slope efficiency 0.25 mW/mA. Figure 20 shows the measured wavelength tuning spectra of a fabricated VCSEL using a bridge nanomechanical actuator. The laser is biased at ∼1.2 times the threshold current and actuated under various applied voltages across the tuning contact. An 18 nm continuous wavelength tuning is obtained with 0–6 and 9–14 V of external applied voltage. One stop is observed at 6–9 V due to the phase mismatch
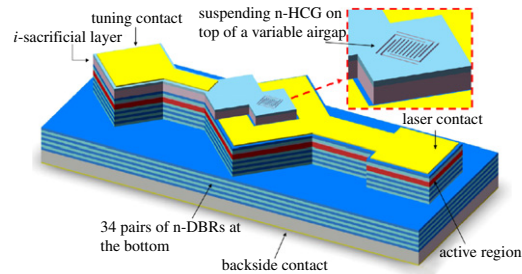
Schematic of tunable VCSEL, consisting of an n-doped HCG top mirror, a sacrificial layer, two pairs of p-doped DBRs, an AlGaAs oxidation layer, a cavity layer containing the active region, and a bottom standard n-doped DBR mirror. Electrical current injection is conducted through the middle laser p-contact and back side n-contact. An aluminum oxide aperture is formed on the AlGaAs layer just above the active region to provide current and optical confinement. The HCG is freely suspended above a variable air gap and supported via a nanomechanical structure. The tuning contact is fabricated on the top n-doped HCG layer [16].

between the HCG and VCSEL cavity. This stop can be eliminated with an optimized air gap.

Figure 21 shows the relative optical tuning response from the mechanical tuning of the HCG measured by applying a sinusoidal AC modulating voltage in addition to a DC voltage, while the VCSEL is injected with constant current. For a 3 μm × 3 μm HCG with 3 μm long membrane bridges, the 3 dB frequency is as high as 27 MHz, with an equivalent tuning time of 18 ns (inverse of half-cycle). Compared with other DBR-based electrostatic-actuated MEM VCSELs (with tuning speed of ~10 μs), the demonstrated tunable VCSEL with an integrated mobile HCG has a faster wavelength tuning speed by close to 3 orders of magnitude.

3.3b. Tunable Proton-Implanted 1550 nm VCSEL

As discussed in Subsection 3.2a, a proton implant can be used to provide current confinement, since the active region is at a short distance from the top surface. Figure 22 shows a monolithic, tunable 1550 nm VCSEL structure [26]. The detailed design is similar to that described in Subsection 3.2a [19] with the addition of MEMS suspension of the HCG and reconfiguration of the contacts for MEMS [26]. The HCG can be electrostatically actuated toward the substrate, changing the lasing wavelength. Given that the structure requires one single epitaxy and the critical steps are done on a planar wafer, the fabrication process facilitates low-cost, scalable manufacturing.

The VCSELs have excellent performance characteristics. Single-mode operation with a >40 dB side mode suppression ratio is obtained over the temperature range up to 85°C. Tunable VCSELs were realized with a continuous tuning range of 16.5 nm, shown in Fig. 23(a), by using MEMS tuning. The emission wavelength continuously blueshifts with

Figure 20
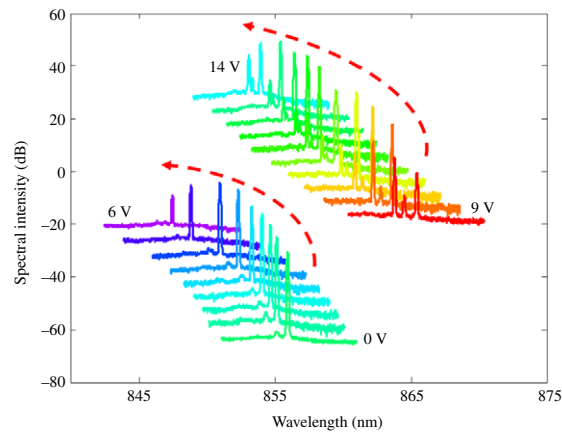
Measured wavelength tuning spectra of tunable VCSEL using a bridge nanomechanical actuator. The laser is biased at ∼1.2 times the threshold current and actuated under various applied voltages across the tuning contact [16].

Figure 21
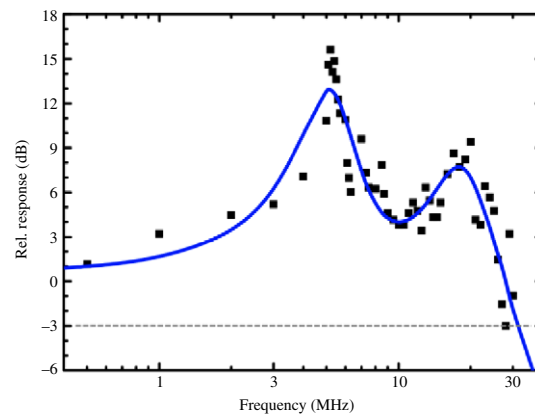
Mechanical response for a 3 μm × 3 μm HCG with 3 μm long membrane bridges. The 3 dB frequency is as high as 27 MHz [17].

increasing MEMS voltage. 16.5 nm of continuous tuning was achieved with 8.5 V, while keeping the bias current at 20 mA. Figure 23(b) shows the maximum output power (blue) and threshold current (red) as a function of wavelength when the device is mechanically tuned from 0 to 8.5 V. The CW optical power is ∼1.5 mW, and the threshold current is under 5 mA over almost the entire mechanical tuning range.

3.4. Multiwavelength Vertical-Cavity Surface-Emitting Laser Array

WDM offers an ideal way to achieve high aggregate bandwidth by using low-cost, low-power-consumption lasers and electronics. Multiwavelength VCSEL arrays are promising sources for dense and
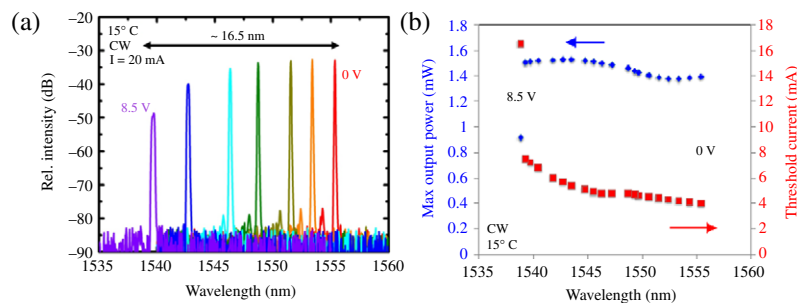
Figure 22
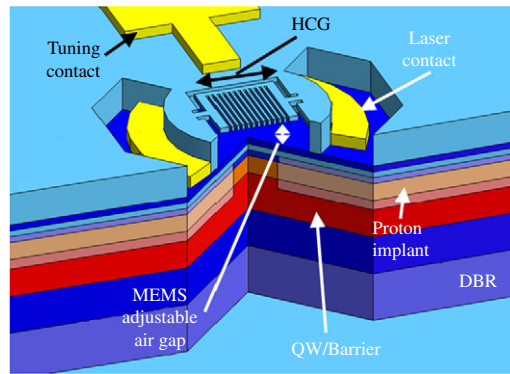
Schematic of tunable proton-implanted VCSEL [26].

Figure 23

(a) Mechanical tuning range of a tunable HCG VCSEL. The laser lases over a range of 16.5 nm. (b) The maximum output power (blue) and threshold current (red) as a function of the wavelength. The device outputs over 1.5 mW over most of the mechanical tuning range [26].

coarse WDM optical interconnects. The first multiwavelength VCSEL array was proposed and demonstrated by varying the thickness of several layers of the VCSEL cavity during epitaxial growth [86], which changes the cavity round-trip path length, and thus lasing wavelength. Many other approaches have been reported ever since [87–89].

Here we discuss two methods to achieve multiwavelength HCG VCSEL arrays. The first one uses the same HCG for the array. The laser wavelength is varied by changing the distance between the HCG reflector and the rest of active region [25]. This design principle is similar to that of the tunable VCSEL. We experimentally demonstrate CW room temperature operation of an HCG VCSEL array with wavelength range over 50 nm.

The second approach leverages an interesting dependence of the phase of the reflection coefficient on the HCG bar width [32]. Since the VCSEL wavelength is determined by the round-trip 2π phase condition, as in any FP cavity, a large VCSEL wavelength range can be obtained with the same epitaxy, i.e., same *HCG and cavity layer thicknesses*, by simply

Figure 24
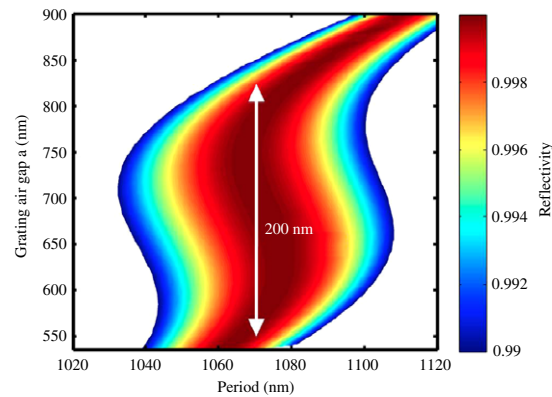
Simulation of HCG reflectivity by RCWA. The design tolerance of the HCG is calculated at a fixed wavelength of 1550 nm, and the grating air gap variation could be $> \pm 100$ nm [25].

varying the HCG period and duty cycle lithographically. Theoretical simulation shows that a wide range, in excess of 100 nm, can be achieved.

3.4a. Multiwavelength 1550 nm Vertical-Cavity Surface-Emitting Laser Array Using Varied Optical Cavity Length

The full VCSEL cavity used here is the same as that described in Subsection 3.2a. The lasing wavelength is determined by the optical path length between the two mirrors and the phases of the HCG and bottom DBR. The factors limiting VCSEL wavelength range are gain bandwidth, DBR reflectivity bandwidth, and optical confinement factor. TE HCG is used with dimensions $\Lambda =\sim 1070$ nm, $a =\sim 700$ nm, and $t_g = 195$ nm. The HCG design here was optimized so that it is highly tolerant to errors in the grating air gap, the most difficult value to control in HCG fabrication. This design shows a tolerance to $>\pm100$ nm in air gap variation, as shown in Fig. 24. The trade-off for the tolerance is bandwidth, but by adjusting the HCG dimensions, a bandwidth >100 nm can be obtained.

HCG VCSELs were fabricated with steps similar to those in Subsection 3.2a. Figure 25(a) shows the light–current characteristics of these devices with different optical cavity lengths, and Fig. 25(b) shows the optical spectrum at a fixed current of 10 mA. Some variation in output power and threshold current is seen in the devices. This is likely due to a lack of uniformity in the HCG and other fabrication-related variations as well as the wavelength dependence of gain. With further fabrication optimization, more uniform device characteristics are expected regardless of the lasing wavelength. Devices were obtained with output wavelengths ranging from 1540 to 1591 nm. This is the first experimental verification that the HCG is reflective enough for a VCSEL to lase over such a broad wavelength range (>50 nm).

Figure 25
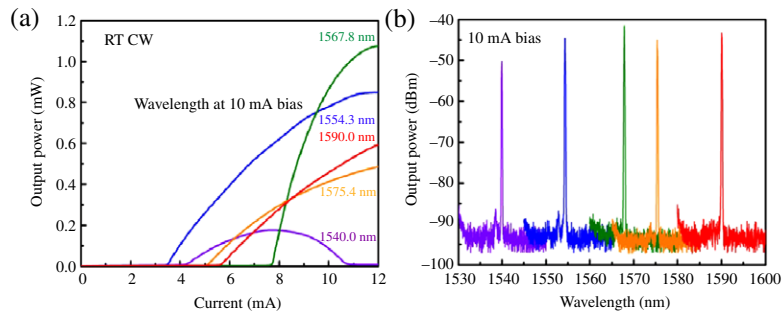
(a) Light–current curve and (b) spectrum of multiwavelength HCG VCSELs under CW operation at room temperature. All the devices in (b) are biased at 10 mA, and the wavelength range is from 1540 to 1591 nm [25].

Figure 26
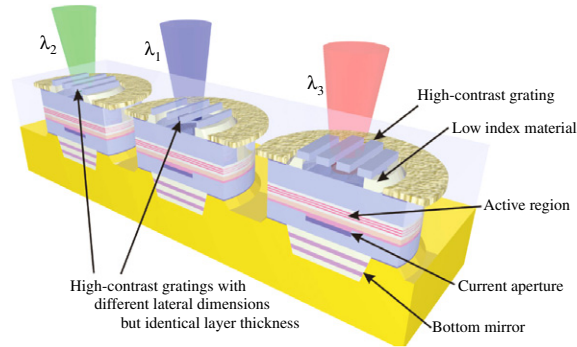
Schematic of multiwavelength VCSEL array. The lasers have the same epitaxy, including HCG thickness. The VCSEL wavelength is changed by varying the HCG period and duty cycle [32].

3.4b. Using High-Contrast Grating Dimension to Control Wavelength

In Section 2, we showed that the magnitude and phase of the reflectivity coefficient can be controlled by the propagation constants of the HCG waveguide array mode, β_m. In addition, the β_m values are determined primarily by the semiconductor bar width s. Hence, the phase of the reflection coefficient can be varied by the HCG dimension while maintaining nearly 100% reflection. This property can be used to control the VCSEL emission wavelength [32] as well as to make lenses [33,34], which will be discussed in Section 4.

Figure 26 shows the schematic for a VCSEL array using identical epitaxial structures while emitting different wavelengths based on different HCG periods and duty cycles. The VCSEL structure used for this simulation is similar to that reported in [66], with the epitaxial top mirror being replaced by an HCG.

In Fig. 27(a) we show reflectivity, and in Fig. 27(b) phase spectra, for HCGs with the same thickness t_g but various combinations of

Figure 27
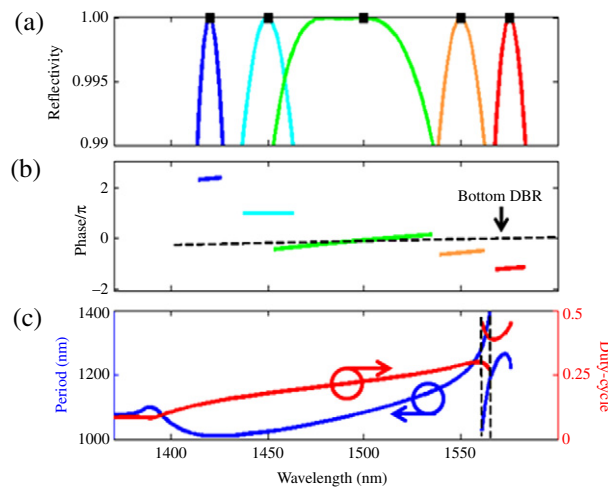
(a) Magnitude and (b) phase of reflectivity spectra of HCGs with different periods and duty cycles in (c), keeping the same HCG thickness.

period Λ and duty cycle η. A relatively *thick* HCG, 900 nm, is used to achieve a larger phase variation. This can be understood, since a longer propagation length facilitates more interference effects. This leads to the possibility of significantly changing the lasing wavelength by using moderate changes in HCG lateral dimensions. Figure 27(c) shows the corresponding VCSEL cavity wavelength. The wavelength range would eventually be limited by the bandwidths of the gain region and the bottom DBR. However, if those were not limiting factors, a very wide cavity wavelength range of 100 nm could be achieved.

4. Resonator with Surface-Normal Optical Coupling

High-quality-factor (Q) optical resonators have attracted much attention with their various applications, which include lasers, single-photon sources, optical filters, and sensors [90–95]. Various structures have been used to form high-Q resonators, including microdisks, photonic crystals, ring resonators, DBRs, and distributed feedback (DFB) structures [90,91,96–98]. Most of them employ a collinear configuration for the resonant optical mode and optical output. While such a configuration facilitates device integration in a cascaded fashion, it does not facilitate simple coupling with fiber or free-space optics. A high-Q resonator with surface-normal emission is of great interest for many applications, such as lasers, optical filters, and sensors.

As mentioned in Section 2, an HCG can naturally form high-Q resonances with surface-normal emission. In this section, we will provide a review of preliminary experimental results of a simple high-Q resonator [30]. We will also discuss a new design with double resonance for surface-enhanced Raman scattering (SERS) sensing applications [31].
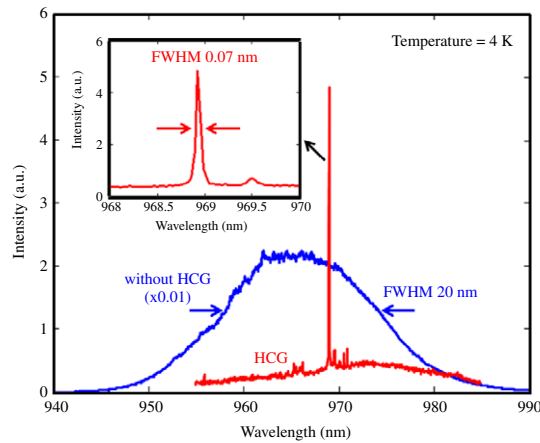
Emission spectrum of HCG resonator (in red) and emission spectrum in the area without grating (in blue). The inset shows an enlarged picture of the HCG emission spectrum. The FWHM of the HCG resonator emission peak is ~0.07 nm, and Q is ~14000 [30].

4.1. High-Q Resonator

The design of a TE HCG resonator demonstrated in [30] includes an $Al_{0.6}Ga_{0.4}As$ layer with three $In_{0.2}Ga_{0.8}As$ quantum wells in the center. The device was grown by metal organic chemical vapor deposition (MOCVD) on a GaAs substrate. Underneath this HCG layer is an air gap, with a 20-pair bottom-DBR to provide extra reflection. The HCG has dimensions Λ, t_g, and η equal to 502 nm, 385 nm, and 64%, respectively. The QW emission wavelength is ~980 nm, and the refractive index of the HCG layer is 3.15. This resonance is basically M_{20}, the lowest-order anticrossing shown in Fig. 11(b), although the duty cycle used here is not exactly the same. The grating structure was patterned by electron-beam lithography and etched by reactive ion etching. A wet chemical-based selective etching followed by critical point drying was used to remove the sacrificial material underneath the HCG layer and form the freely suspended grating.

The resonator is experimentally demonstrated, depicted in Fig. 28. Low-temperature (4 K) photoluminence was measured by using a Ti:sapphire laser at 800 nm wavelength. The emission spectrum of the wafer without the HCG resonator structure is plotted in blue in Fig. 28, showing a typical photoluminence spectrum of the InGaAs quantum wells with a FWHM linewidth of 20 nm. The HCG resonator emission is shown as the red curve in Fig. 28. A very narrow photoluminence emission linewidth is obtained. The inset shows the enlarged emission with a FWHM linewidth as narrow as 0.07 nm, which is limited by our spectrometer resolution. This translates to a Q factor as high as 14,000. With increasing pumping power, no further narrowing of the spectrum was observed. This is because of the spatial mismatch of the QW position, which is at the center of the HCG grating bars, and resonator intensity peak at the edge of the grating bars.
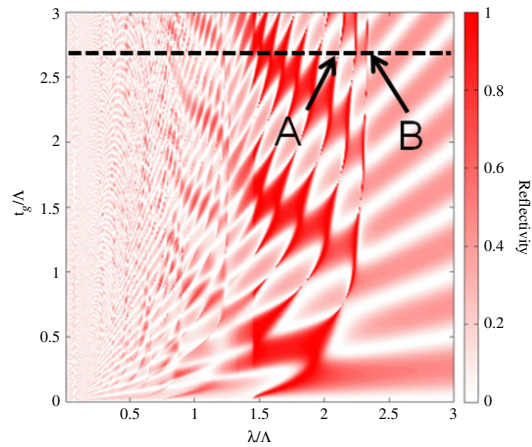
The TE HCG t_g–λ reflectivity contour plot with the locations of resonances used in the SERS enhancement structure (Fig. 30). The horizontal dashed line $t_g/\Lambda = 2.70$ cuts across various resonance points. Point B is M_{70} resonance, used to enhance the Raman signal, whereas point A is M_{82}, using for the pump laser. The silicon HCG is half-buried in the oxide substrate. Liquid containing the sensed molecules is placed on top of the grating structure. Its refractive index is $\sim$1.33. $\eta = 0.6$ for the HCG.

4.2. Double Resonator for Simultaneous Enhancement of Pump and Probe

SERS is a powerful sensing mechanism that has the potential of facilitating label-free single-molecule detection [99]. Typically, rough metal surfaces are used to provide field enhancement. However, in an effort to provide spatial control on the field-enhancement locations ("hot-spots"), it was proposed to replace the inhomogeneous rough surface by lithographically defined nanoantenna arrays [100]. The main limitation of such a method is that hot-spot locations are then limited to the dipole gaps of nanoantennae, which obviously occupy an exceedingly small fraction of the overall volume. To compensate for the low volumetric coverage, techniques of embedding the nanoantenna inside optical resonators have been proposed. Since the overall SERS signal is proportional to the product of the pump and the Raman signal, it is desirable to design an optical resonator that can provide field enhancement for both the pump and the SERS signal. Here, we review an HCG resonator design that can enhance both optical signals at the same physical location to improve the overall SERS signal by several orders of magnitude [31].

It is possible to find an optimized parameter set such that one HCG can exhibit several resonances at different wavelengths. This can be seen in Fig. 29, where three resonances, M_{70}, M_{81}, and M_{82} are obtained for the same thickness $t_g/\Lambda = 2.70$. Their resonance order is first, second, and third, respectively. For SERS applications, not only do the resonance wavelengths need to be in specific ratio, representing the pump and Raman signal of interests, but the field intensity peaks must be at the
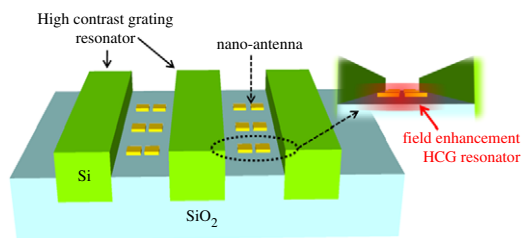
Proposed structure for SERS application. The HCG is half-buried in the oxide substrate in order to benefit from its odd-order resonances, all of which facilitate field enhancement at the center plane of the HCG thickness. The nanoanennae will then be lithographically defined at the grating gaps [31].

same physical location. To achieve this, we need to understand the field distribution of the HCG resonances.

The resonances of the HCG can be characterized by their order, as discussed in Subsection 2.3c. For SERS applications, the HCG resonances need to exhibit an intensity peak at the $z = t_g/2$ plane at the center of the gap between the gratings. The M_{70} and M_{82} resonances are used for the Raman and pump signals, labeled B and A, respectively, in Fig. 29. The nanoantennae are therefore placed at the HCG center plane, as shown in Fig. 30, which is achieved by half-burying the (Si) HCG in a low-index (SiO_2) substrate. The structure shown in Fig. 30 is then immersed into a liquid containing the sensed molecules. The refractive index difference between the oxide substrate below ($\sim$1.46) and the liquid above ($\sim$1.33) is not substantial enough to significantly break the symmetry and detune the intensity peak from the center plane. Figure 31(a) shows the M_{82} resonance (third-order HCG resonance, i.e., three intensity peaks across the HCG thickness) intensity profile designed at the pump wavelength, and Fig. 31(b) the M_{70} resonance (first-order HCG resonance) intensity profile designed at the Raman signal. Their intensity enhancement at the HCG center plane is $\sim$$10^4$ and $\sim$$10^2$, respectively, even before the nanoantennae are introduced into the structure. The intensity enhancement in Fig. 31 is calculated analytically, assuming a surface-normal plane wave incidence. The analytical method of HCG calculations is described in detail in Ref. [44]. In addition, the intensity peaks in Fig. 31 are located between the grating bars, rather than inside the bars; this allows the sensed molecules to easily have access to the hot spots.

Figure 32 shows typical measured Raman spectrum of a *trans*-1,2-*bis*(4-pyridyl)-ethylene (BPE) molecule as the design target for the HCG resonator. The resonance that enhances the pump peak must be high *Q*, since the pump is exceedingly narrowband, while the resonance that enhances the Raman signal should be broad enough to engulf at least one of the Raman peaks. Such design is presented in Fig. 32 (blue), without the nanoantenna. The pump is shown to be enhanced by 4 orders of magnitude (intensity) while the second Raman peak is enhanced by 2 orders of magnitude. The M_{81} resonance (second-order HCG resonance)

Figure 31
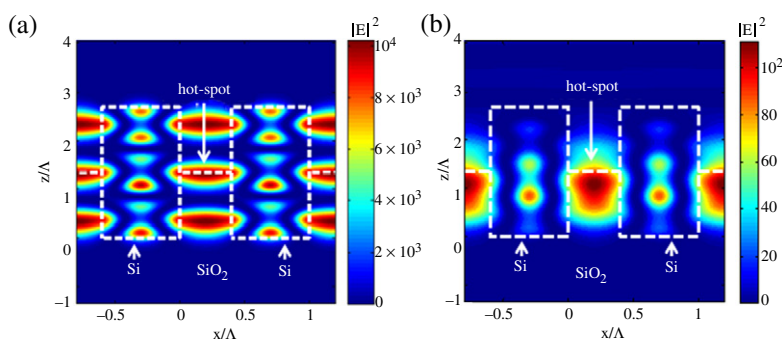
Intensity profile, calculated by using FDTD, for (a) M_{82} HCG resonance (third-order resonance) designed for the pump, point A in Fig. 29, and (b) M_{70} HCG resonances (first-order resonance) designed for the Raman signal, point B in Fig. 29. The intensity peaks are at the HCG center plane in both cases. We chose the dimensions so that the intensity peaks are at the gaps, rather than inside the semiconductor bars, which will make it easy for the molecules to have access to the hot spots. For the third- and first-order resonance, the peak enhancements are ~10^4 and 10^2, respectively. HCG parameters are $\Lambda = 372$ nm, $t_g = 1003$ nm, and $\eta = 0.6$. Wavelength is 785 nm for the pump. Light is TE polarized. The Raman shift is 1197 cm^{-1}. Liquid containing the sensed molecules is placed on top of the grating structure. Its refractive index is ~1.33 [31].

in Figs. 29 and 32 will not interact with the BPE molecule, since it has a null at the HCG center plane.

The paradigm described above tacitly assumed that the enhancement provided by the HCG resonator will simply multiply the enhancement in the nanoantenna gaps, thus increasing the overall signal by an appropriate number of orders of magnitude. Such linear behavior is an idealized assumption, and it requires validation. Figure 33 shows such validation using FDTD simulation. Figures 33(a), 33(b) and 33(c) show the enhancement spectra of the entire structure, nanoantenna alone, and HCG only, respectively. Indeed the overall intensity enhancement is greater than 10^5, which agrees well with the simple multiplication of individual enhancements by pump and Raman. The only deviation is a slight frequency shift of the combined enhancement in Fig. 33(a), but it can be easily compensated for by slight scaling of HCG dimensions, such that the overall resonance still matches the targeted BPE peak.

5. Planar High-Numerical-Aperture Focusing Reflectors and Lenses

Focusing reflectors and lenses are among the most fundamental components in optics. An HCG can be designed to be an ultrathin planar lens and focusing reflector [33–35]. The figures of merit of focusing lens or reflector include the numerical aperture (NA), power handling capability, thickness, aberration, transmittance, reflectance, and

Figure 32
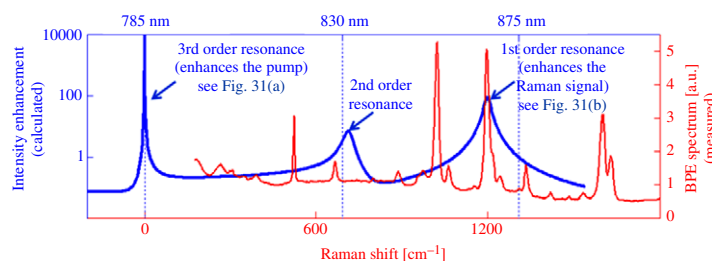
Intensity enhancement spectrum of HCG overlaid on the Raman spectrum of the BPE molecule, measured under a 785 nm pump. The M_{82} resonance (third-order resonance) is high Q, and it enhances the pump by 4 orders of magnitude. The M_{70} resonance (first-order resonance) is broader, in order to engulf the Raman peak [31].

Figure 33
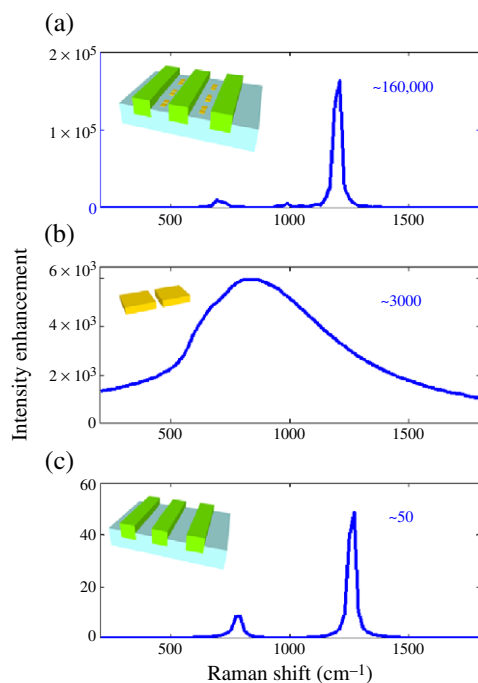
FDTD simulation of intensity enhancement of (a) the entire structure (HCG + nanoantenna), (b) nanoantenna only, and (c) HCG only. The intensity enhancement of the entire structure is $> 10^5$ at the Raman wavelengths, agreeing well with simple multiplicative dependence on the individual enhancements of the HCG and nanoantenna. Nanoantenna dimensions are as follows: dipole gap 11 nm, thickness 32 nm, width 32 nm, and length 210 nm [31].

potential novel functions. The NA is one of the most critical performance metrics because it indicates the focusing or resolving power of the reflector or lens. The focusing capability of conventional bulk lenses and reflectors arises from their aspherical shape, which present difficulties for microfabrication and chip-scale integration. Zone plates and Fresnel

lenses are attractive because they are planar and compact. A zone plate consists of a set of radially symmetric rings that are alternately opaque and transparent, harnessing diffraction to create a lensing effect [101,102]. The major drawback of zone plates is that they absorb a significant part of the input power [102]. A Fresnel lens consists of many concentric segments with continuous height variations [103–106]. However, Fresnel lenses must trade off the number of height steps, and the resulting fabrication complexity, with NA or focusing power.

Recently, our group reported an HCG design algorithm for focusing reflectors with 0.81 NA and 0.3 dB loss and a lens with 0.96 NA and 0.2 dB loss [33]. Fattal *et al.* reported a 2D lens using Si with a thin layer [34,35]. Such structures are simple to fabricate with standard photolithography and may be readily incorporated into a variety of integrated electronic and photonic platforms. We review the design algorithm briefly below.

Designing HCG focusing elements can be done first with a spatial phase distribution obtained from simple geometrical argument, given a desired focal length and NA:

$$\phi(x) = \frac{2\pi}{\lambda}\left(f + \frac{\phi_{max}}{2\pi}\lambda - \sqrt{x^2 + f^2}\right), \tag{23}$$

where f is the focal length, λ is the wavelength, and ϕ_{max} is the maximum phase change (the phase difference between the center and the very edge of an HCG). When the phase $\phi(x)$ is more than 2π, it can be mapped to an equivalent value between 0 and 2π. The solid trace in Fig. 34(a) shows such an example, with each sawtooth corresponding to a different 2π window. Next, we recognize that a chirped HCG with different bar widths and gaps can provide a discrete phase distribution to approximate the ideal continuous distribution [shown in the green circles in Fig. 34(a)].

The next step is to find a one-to-one correspondence between the HCG's dimensions and complex reflection or transmission coefficients. As an example, let us consider HCG focusing reflector design here. The reflectivity and phase calculated as a function of HCG dimensions by RCWA is shown in Fig. 34(b) with 1.2 μm thickness, which has been optimized to obtain high reflectance and large phase change. The bar width varies from 0.25 to 0.75 μm, and the air gap between bars from 0.1 to 0.6 μm. The actual dimensions chosen for an HCG reflector design are shown on this map as a series of circles, colored according to their corresponding 2π window [Fig. 34(a)]. The design is for TM polarization at 1.55 μm wavelength. The *H*-field intensity (normalized by incident field intensity) on both the reflection side and the transmission side is plotted in Fig. 35(a). The plane wave, incident from the positive *z* half-plane, is mostly reflected by the 28.6 μm wide HCG reflector and focused to a spot 10.3 μm above the lens, yielding an NA of 0.81. The total reflectance is 93%, which means the transmission loss is only 0.3 dB. The intensity oscillations on the reflection side along the *z* axis in Fig. 35(a) are caused by interference between the reflected and incident waves. At the reflection focal plane, the field distribution is shown in Fig. 35(b), with a FWHM of 0.86 μm, which is extremely close to the diffraction limit. This field distribution is plotted after the incident wave is subtracted from

Figure 34
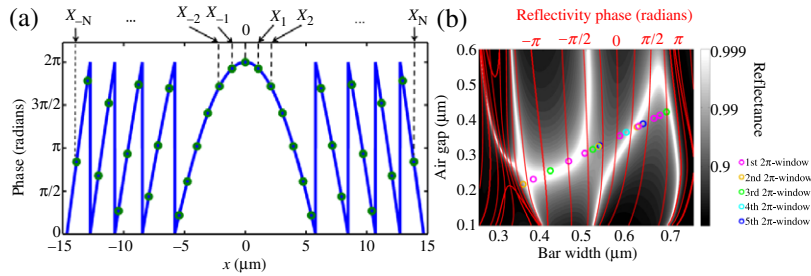
(a) Phase distribution $\phi(x)$ for a lens, with each sawtooth corresponding to a different 2π window. A chirped HCG with different bar widths and gaps can provide a discrete phase distribution to approximate the ideal continuous distribution (green dots). (b) The reflectivity and phase calculated as a function of HCG dimensions with 1.2 μm thickness. The actual dimensions chosen for an HCG reflector design are shown on this map as a series of circles, colored according to their corresponding 2π window in (a) [33].

Figure 35
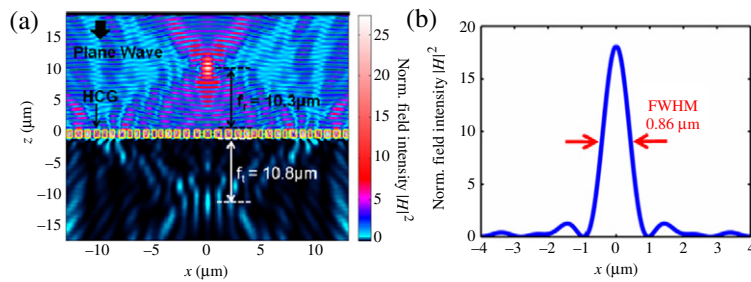
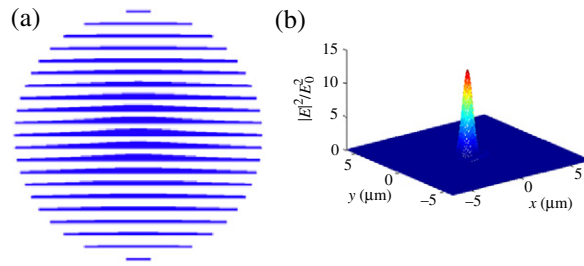

(a) H-field intensity distribution (normalized by incident field intensity) on both the reflection side and the transmission side of an HCG focusing reflector. HCG bars are denoted by yellow boxes (b) H-field intensity distribution (normalized by incident field intensity) at the reflection focal plane. This field distribution is plotted after the incident wave is subtracted [33].

the total field intensity. It is most interesting to note that although the reflection map is calculated for periodic HCGs, somewhat surprisingly, its use in arriving at a design for a nonperiodic chirped HCG reflector is excellent, as shown by FDTD simulations in Fig. 35(a).

A unique phenomenon of the HCG reflector is "double focusing." As can be seen in Fig. 35(a), not only is the reflected wave focused, but also the transmitted wave, even though the transmitted energy is much lower. Moreover, the focal length on the transmission side is 10.8 μm, almost the same as that of the reflection side. This effect is due to the relationship between reflection and transmission phase for a lossless, reciprocal, symmetric system [107],

$$\phi_R - \phi_T = \frac{\pi}{2} + m\pi, \quad m = 1, 2, \ldots, \tag{24}$$

Figure 36

(a) Top view of a 2D HCG lens designed by varying bar width and air gap. (b) A 3D FDTD simulated E-field intensity distribution of the output at the focal plane with a Gaussian beam as input source. The Gaussian beam is focused from 3.5 μm (waist radius) down to 0.89 μm, a 15X reduction in area [33].

where ϕ_R and ϕ_T are the phase of reflection and transmission, respectively. This relation is confirmed by calculating the phase of reflectivity and transmissivity for our planar HCGs. Since the difference is either $\pi/2$ or $3\pi/2$, the phase distributions on either side of the HCG can be made nearly the same with possible discontinuities with a phase jump of π. In fact, for the case in Fig. 35, $\phi_T(x)$ is nearly the same as $\phi_R(x)$, leading to the double focusing. The capability to realize a planar focusing reflector with an additional focus on the transmission side is a unique property of HCGs. It will revolutionize the design of VCSELs, vertical-external-cavity surface-emitting lasers, or solid-state lasers, where a single HCG reflector can be used as a cavity mirror providing optical confinement and an external coupling–focusing element. Similar to the reflecting focusing element, an HCG lens can also be designed for TM polarization with an NA of 0.96 and 95% transmittance with a FWHM of 0.65 μm [33].

A 2D HCG lens can be easily designed by varying the bar width and air gap inside each HCG period. A simple illustration is shown in Fig. 36(a). In this case, the diameter of the 2D HCG lens is 10 μm and the HCG thickness is 3 μm. A 3D FDTD simulation is performed for a Gaussian beam source. The lens is designed for TE polarization, and the E-field intensity distribution of the focal plane is shown in Fig. 36(b). The lens focuses the incident beam from a 3.5 μm waist radius down to only 0.89 μm, increasing the peak intensity more than 12 times. We expect that, by using a bar-by-bar optimization scheme where the dimension of each bar is further adjusted to maximize the total transmission, the focused spot intensity can be increased.

6. Discussion

Thus far, we have summarized theoretical and experimental results on HCG properties with surface-normal incidence. It is natural to question if the extraordinary properties can be obtained with the more general case of oblique incidence where $\theta \neq 0$ (Fig. 1). Can a broadband mirror, transparent window, or high-Q resonator be obtained with light incidence at an angle to one ultrathin layer of grating? This is important for designing

optics with specific angular distribution. It is also interesting to examine HCG properties as the incident angle approaches 90°and the HCG looks more and more like a conventional DBR or 1D photonic crystal. In this section, we answer these two questions and present really intriguing connections between HCGs and photonic crystals.

6.1. Oblique Incidence

With surface-normal incidence, only even modes are excited inside HCG (i.e., TE$_0$/TM$_0$, TE$_2$/TM$_2$, etc.). For a plane wave with oblique incidence, however, the odd modes will also be excited. Hence, we must add the sinusoidal terms in $\mathcal{H}_{y,m}^{\mathrm{II}}(x)$ and $\mathcal{E}_{x,m}^{\mathrm{II}}(x)$ in Eq. (2b). Second and most important, the periodic boundary condition in Eq. (2c) becomes the Bloch boundary condition,

$$\mathcal{H}_{y,m}^{\mathrm{II}}(x + l\Lambda) = \mathcal{H}_{y,m}^{\mathrm{II}}(x)e^{ik_{x0}l\Lambda}, \quad l \text{ is an integer,}$$

$$\mathcal{E}_{x,m}^{\mathrm{II}}(x + l\Lambda) = \mathcal{E}_{x,m}^{\mathrm{II}}(x)e^{ik_{x0}l\Lambda}, \quad l \text{ is an integer}$$

$$k_{x0} = k_0 \sin\theta = \frac{2\pi}{\lambda}\sin\theta. \tag{25}$$

Here k_{x0} is the plane wave propagation constant (k_0) projected in the x direction. In other words, the waveguide array modes must also propagate in the x direction with a propagation constant k_{x0} in region II, in order to fulfill the boundary conditions.

The modes in regions I and III would also include both even and odd modes, or, more generally, they can be expressed in the form $e^{ik_{xn}x}$, where k_{xn} is the k-vector in the x direction for different diffraction orders. With a similar equations setup as Eqs. (1)–(9), the reflectivity and transmission properties as well as the mode profile of the whole system can be obtained.

Figure 37 shows the reflectivity contour plot for a TE HCG as a function of wavelength and grating thickness, at an incident angle $\theta = 50°$. Clear checkerboard patterns are observed, indicating that the same phase selection rule applies here. The resonance curves for the zeroth-, first-, second-, and third-order (super)modes are clearly seen.

There are two differences from the surface-normal case. First, the dual-mode region is operated with the zeroth- and first-order mode for $\lambda_{c2} < \lambda < \lambda_{c1}$, instead of zeroth- and second-order mode for $\lambda_{c4} < \lambda < \lambda_{c2}$. Compared with the second-order mode, the first-order mode has a longer cutoff wavelength, and thus the dual-mode region is shifted to a longer wavelength. Second, the diffraction region is $\lambda_D \leq (1 + \sin\theta)\Lambda$ instead of $\lambda_D \leq \Lambda$, which can be clearly seen by a sudden change of reflectivity at $\lambda/\Lambda = 1.77$ in Fig. 37. The diffraction regime can be expressed in frequency:

$$\omega_D / \left(\frac{2\pi c}{\Lambda}\right) \geq 1 - k_x / \left(\frac{2\pi}{\Lambda}\right). \tag{26}$$

Similar to the surface-normal case, when two resonance curves intersect, either anticrossing or crossing phenomena happen depending on their

Figure 37
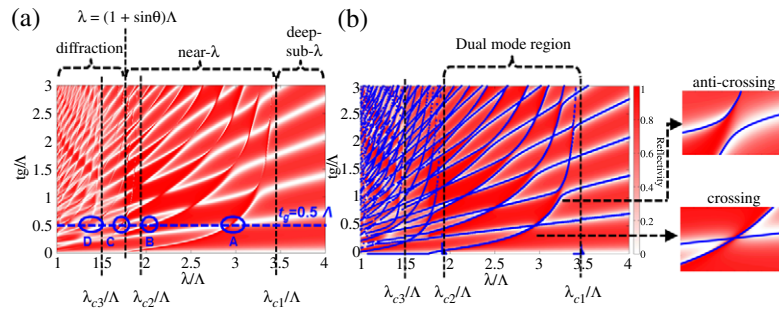
(a) Reflectivity contour of an HCG as a function of wavelength and grating thickness. The incident wave is TE polarized, with an incident angle $\theta = 50°$. The mode cutoffs ($\lambda_{c1}, \lambda_{c2}, \lambda_{c3}$) as well as the first-order diffraction cutoff lines are marked to clearly illustrate the three wavelength regimes: deep-subwavelength, near-wavelength, and diffraction. (b) Analytical solutions of FP resonance conditions of the individual modes [Eq. (11), but for oblique incident angle], shown by the blue curves, superimposed on the reflectivity contour in (a). Excellent agreement is obtained between the analytical solutions and the simulation results. The insets show examples of an anticrossing and a crossing of the FP resonance lines (blue curves). HCG parameters are $\eta = 0.6$, $n_{bar} = 3.48$, TE polarization, and $\theta = 50°$. In Subsection 6.2, the HCG band diagram will be discussed. Figure 37(a) is used to illustrate how to extract the band diagram. A horizontal line $t_g = 0.5\Lambda$ is plotted for the chosen thickness, which cuts across various resonance curves of different modes. The crossing point regions are labeled A–D. In region A, $t_g = 0.5\Lambda$ crosses first- and zeroth-order resonance; in region B, first-order resonance; in region C, second- and zeroth-order resonance; in region D, first-, second-, and third-order resonance. The incident angle is then varied from 0° to 90°, and these crossing points can be traced along the wavelength, forming a photonic band, as shown in Fig. 38(a). See Subsection 6.2 for more discussion.

parity. This shows that HCG under oblique incidence still possesses the same extraordinary properties as those under surface-normal incidence. Indeed, one ultrathin layer of grating can result in ultrabroadband reflection, transmission, or a high-Q resonator regardless of incidence angle. This is a direct consequence of the high index contrast and near-wavelength period.

6.2. Relationship to One-Dimensional Photonic Crystals

At first glance, an HCG looks no different from a DBR or 1D photonic crystal. On the other hand, one can see a wealth of extraordinary properties that were not discovered in photonic crystals. We showed that the unique characteristics of HCG come from the rich interactions of the waveguide array modes. The most intriguing of all is the strong dependence on HCG thickness and duty cycle, which distinguishes HCG from photonic crystals or other gratings. For the HCG theory, we consider incident waves coming from region I and having a real propagation constant (k_z) in the z direction [$k_{x0} < k_0$ in Eq. (25), and thus

$k_z^2 > 0$ in region I with $k_{x0}^2 + k_z^2 = k_o^2$]. In photonic crystals, on the other hand, the typical consideration is for waves incident and propagating in the x direction, while exponentially decaying in the z direction [$k_{x0} > k_0$ in Eq. (25), and thus $k_z^2 < 0$ in region I]. Hence, an HCG and a 1D photonic crystal can be unified with the same theoretical architecture and band diagram, and the two of them are distinguished from each other by operating under different conditions.

To illustrate this, we choose a specific HCG thickness and duty cycle and calculate the HCG reflectivity versus different optical frequencies and incident angles. With the incident angle subsequently converted into a k_{x0} value, the HCG reflectivity is plotted in Fig. 38(a) versus frequency and k_{x0} (for simplicity, we label k_{x0} as k_x in this section). This is essentially a band diagram with different photonic bands illustrated, with lines across which sharp reflectivity change happens or lines with full transmission. With careful analysis and comparison with the more familiar reflectivity contour plot versus wavelength and HCG thickness in Fig. 37(a), we can associate these different photonic bands with the mth-order supermode resonance in HCG. Note that only the photonic bands above the light line can be calculated, simply because we use a plane wave to excite these modes from the top of the HCG (i.e., region I in Fig. 3). These discrete bands above the light line shown here indicate the resonating conditions, where high Q can be achieved. One interesting result from Fig. 38(a) is that an HCG can be designed to have a very wide-angle high reflection or transmission in a certain wavelength range.

Alternatively, a full band diagram can be obtained by FDTD simulation with the Bloch boundary condition on a single HCG period (i.e., HCG unit cell), by using the conventional procedure of placing random dipole sources in the unit cell to excite all possible modes. Shown in Fig. 38(b), the band diagram is plotted from $k_x = 0$ to $2\pi/\Lambda$, which is symmetric between $k_x = \pi/\Lambda$ because of Brillouin zone folding. Above the light line, this diagram shows exactly the same band structures as in Fig. 38(a). This strongly indicates that the photonic bands originate from the resonance of the HCG supermodes. Below the light line lie the bands typically seen in a (1D) photonic crystal [108], where the modes are *guided* along the x direction in the photonic crystal. Given that the band is continuous across the light line if it appears both above and below the light line, the HCG supermode resonance can be used to signify the whole photonic band, not only above the light line, but also below the light line!

Figures 38(a) and 38(b) provide an intuitive physical insight into the photonic bands: the mth-order band originates from the mth-order HCG supermode resonating in the z direction. Note that the resonance condition for the mth-order HCG supermode is $\psi_m = n\pi$ [Eq. (11)]. Thus, for the same mth-order HCG supermode and a fixed HCG thickness, there are various FP resonances corresponding to different frequencies ($n = 0, 1, 2, \ldots$). We label these resonances R_{mn}. Correspondingly, in the band diagram [Fig. 38(b)], there would be various subbands belonging to the same mth-order band. The thicker the HCG is, the denser the subbands would be, as a result of a smaller free spectral range.

A special case is when the HCG thickness increases to infinity. This, in fact, is the case for a *pure 1D* photonic crystal. In this case, there are no longer boundaries at $z = 0$ and $z = t_g$ (see Fig. 3), and the

reflection and mode interaction at these boundaries vanish. The HCG supermode resonances in the z direction thus no longer exist, and they reduce themselves to the pure waveguide array modes, which do not propagate in the z direction and, hence, are at cutoff conditions. This is because, for the pure 1D photonic crystal, the typical consideration is that the wave vector in the z direction is zero. Instead of there being a large number of subbands, there would be only one single band for each mth-order mode [Fig. 38(c)]. There is only one wave pattern uniform in the z direction for each mth-order mode, and this exactly corresponds to that single band. In fact, above the light line, this single band for the mth-order mode is the cutoff frequency trace of the mth-order waveguide array modes.

Figure 38(d) summaries the connections between HCGs and photonic crystals. First of all, the diffraction line of Eq. (26) is basically the folded light line that is due to Brillouin zone folding, above which lies the diffraction regime. The HCG operates above the light line but below the diffraction line, whereas photonic crystal typically operates below the light line [108]. We also show the dual-mode regime for the HCG with cutoff frequencies for HCG first-, second-, third-, and fourth-order supermodes. These cutoff frequency traces are exactly the same as the 1D pure photonic crystal bands, as in Fig. 38(c). It is interesting to again point out the very wide dual-mode regime for surface-normal light, which was the origin of all the extraordinary phenomena mentioned in this paper.

This band analysis illustrates that the HCG and the 1D photonic crystal can be analyzed within the same theoretical architecture. The supermode formulism developed for HCGs is more powerful than the FDTD analysis typically used for photonic crystals. It provides not only intuitive physical insights, but also quantitative information on reflection and transmission coefficients. Comparisons between Figs. 38(a) and 38(b) are most revealing: the resonance modes manifest themselves as full transmission, as in a FP resonance, or, most peculiarly, as a sharp transient from high to low reflections and vice versa.

7. Summary

The recent discoveries of HCGs are reviewed. This extremely simple structure has led to a wealth of new properties. The HCGs can serve as broadband high-reflectivity mirrors, windows and high-Q optical resonators for surface-normal and oblique angle incidence. They are distinctive and different from typical reflectors formed by distributed reflection. The HCG can be explained by waveguide array modes and their interference due to abrupt index change with the exit and input planes. Thus, the HCG's thickness is one of the most important design parameters, since it determines the interference effect. This is a unique feature of the HCG, in sharp contrast to diffraction gratings, guided mode resonances, Wood's anomaly, and photonic crystals. A number of designs and experimental demonstrations of optoelectronic devices are discussed, including VCSELs, tunable VCSELs, and high-Q optical resonators. In addition, we show that the optical phase can be strongly influenced by grating duty cycle. Utilizing this effect, planar focusing

Figure 38
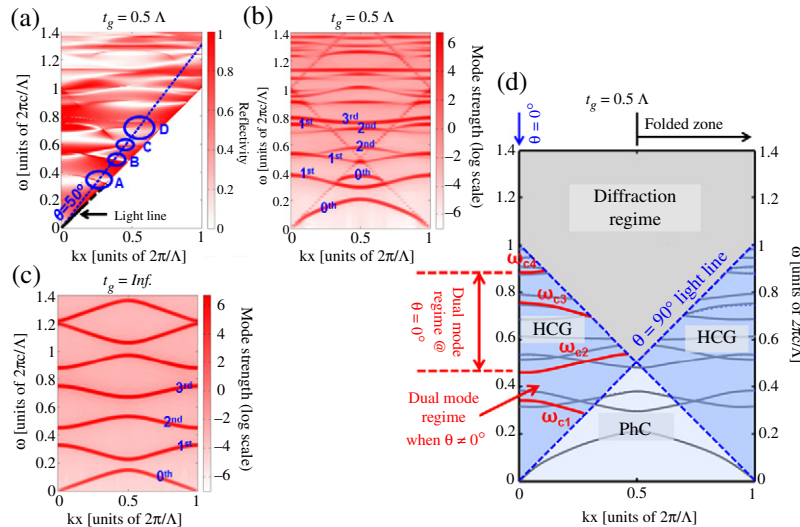
Band diagram analysis of HCG and 1D photonic crystal. (a) HCG band diagram calculated with HCG analytical solution, for $t_g = 0.5\Lambda$. The photonic bands are signified with lines across which sharp reflectivity change happens or lines with full transmission. A dashed curve indicating $\theta = 50°$ is plotted and crosses the band. The crossing point regions are labeled A–D, corresponding to those in Fig. 37(a). (b) Full band diagram simulated with FDTD. The bands are symmetric along $k_x = 0.5(2\pi/\Lambda)$ owing to Brillouin zone folding, and the light line is indicated by the dotted lines. In comparison with (a), one can associate different bands with different orders of supermodes in HCG. Because of the low quality factor of the zeroth-order supermodes above the light line, they do not show up clearly above the light line in (b). (c) The FDTD simulated band diagram for a pure 1D photonic crystal, where $t_g = \infty$. (d) Schematic showing the different operation regime for HCG and photonic crystal (PhC), separated by the light line. The bands are extracted from (a) and (b). The diffraction line of Eq. (26) is basically the folded light line due to Brillouin zone folding, above which lies the diffraction regime. The HCG operates above the light line but below the diffraction line, whereas the photonic crystal typically operates below the light line [108]. We also show the dual-mode regime for HCG with cutoff frequencies for HCG first-, second-, third-, and fourth-order supermodes, labeled ω_{c1}, ω_{c2}, ω_{c3}, and ω_{c4}, respectively. HCG parameters, $n_{bar} = 3.48$, $\eta = 0.6$, TE incident polarized light.

reflectors and lenses can be made with high NA. We believe the rich physics of the HCG has established a new platform for novel compact optical devices and facilitation of their integration.

Appendix A

The closed form of $\mathbf{H}_{n,m}$ and $\mathbf{E}_{n,m}$ in Eq. (5a) can be derived with Eqs. (1b), (1d), (2b) and (2d). The following shows the brief derivations and final results.

TM polarization:

$$\mathbf{H}_{n,m} = \Lambda^{-1}(2 - \delta_{n,0}) \int_0^{\Lambda} \mathcal{H}_{y,m}^{\mathrm{II}}(x) \mathcal{H}_{y,n}^{\mathrm{III}}(x) dx,$$

$$\mathbf{H}_{n,m} = \Lambda^{-1}(2 - \delta_{n,0}) \left[\int_0^{a} \mathcal{H}_{y,m}^{\mathrm{II}}(x) \mathcal{H}_{y,n}^{\mathrm{III}}(x) dx + \int_a^{\Lambda} \mathcal{H}_{y,m}^{\mathrm{II}}(x) \mathcal{H}_{y,n}^{\mathrm{III}}(x) dx \right],$$

$$
\begin{aligned}
\mathbf{H}_{n,m} = \Lambda^{-1}(2 - \delta_{n,0}) \Big\{ & \{2\Lambda \cos(k_{s,m}s/2)[-2n\pi \cos(k_{a,m}a/2) \sin(an\pi/\Lambda) \\
& + k_{a,m}\Lambda \cos(an\pi/\Lambda) \sin(k_{a,m}a/2)]\}/(-4n^2\pi^2 + \Lambda^2 k_{a,m}^2) \\
& + \{\Lambda \cos(k_{a,m}a/2)[-2n\pi \cos(k_{s,m}s/2)[\sin(an\pi/\Lambda) \\
& + \sin(n\pi(a - 2\Lambda)/\Lambda)] - k_{s,m}\Lambda[\cos(an\pi/\Lambda) + \cos(n\pi(a - 2\Lambda)/\Lambda)] \\
& \times \sin(k_{s,m}s/2)]\}/(4n^2\pi^2 - \Lambda^2 k_{s,m}^2) \Big\}.
\end{aligned}
\tag{A.1}
$$

$$\mathbf{E}_{n,m} = \Lambda^{-1}(2 - \delta_{n,0}) \left(\sqrt{\frac{\mu_0}{\varepsilon_0}} \gamma_n/k_0 \right)^{-2} \int_0^{\Lambda} \mathcal{E}_{x,m}^{\mathrm{II}}(x) \mathcal{E}_{x,n}^{\mathrm{III}}(x) dx,$$

$$
\begin{aligned}
\mathbf{E}_{n,m} = & \Lambda^{-1}(2 - \delta_{n,0}) \left(\sqrt{\frac{\mu_0}{\varepsilon_0}} \gamma_n/k_0 \right)^{-2} \\
& \times \left[\int_0^{a} \mathcal{E}_{x,m}^{\mathrm{II}}(x) \mathcal{E}_{x,n}^{\mathrm{III}}(x) dx + \int_a^{\Lambda} \mathcal{E}_{x,m}^{\mathrm{II}}(x) \mathcal{E}_{x,n}^{\mathrm{III}}(x) dx \right],
\end{aligned}
$$

$$
\begin{aligned}
\mathbf{E}_{n,m} = & \Lambda^{-1}(2 - \delta_{n,0})(\beta_m/\gamma_n) \Big[\int_0^{a} \mathcal{H}_{y,m}^{\mathrm{II}}(x) \mathcal{H}_{y,n}^{\mathrm{III}}(x) dx \\
& + n_{\mathrm{bar}}^{-2} \int_a^{\Lambda} \mathcal{H}_{y,m}^{\mathrm{II}}(x) \mathcal{H}_{y,n}^{\mathrm{III}}(x) dx \Big],
\end{aligned}
$$

$$
\begin{aligned}
\mathbf{E}_{n,m} = \Lambda^{-1} (2 - \delta_{n,0}) (\beta_m/\gamma_n) \Big\{ & \{2\Lambda \cos(k_{s,m}s/2) \\
& \times [-2n\pi \cos(k_{a,m}a/2) \sin(an\pi/\Lambda) \\
& + k_{a,m}\Lambda \cos(an\pi/\Lambda) \sin(k_{a,m}a/2)]\}/(-4n^2\pi^2 + \Lambda^2 k_{a,m}^2) \\
& + \{\Lambda \cos(k_{a,m}a/2)[-2n\pi \cos(k_{s,m}s/2)[\sin(an\pi/\Lambda) \\
& + \sin(n\pi(a - 2\Lambda)/\Lambda)] \\
& - k_{s,m}\Lambda[\cos(an\pi/\Lambda) + \cos(n\pi(a - 2\Lambda)/\Lambda)] \\
& \times \sin(k_{s,m}s/2)]\}/[n_{\mathrm{bar}}^2(4n^2\pi^2 - \Lambda^2 k_{s,m}^2)] \Big\}.
\end{aligned}
\tag{A.2}
$$

TE polarization:

$$\mathbf{H}_{n,m} = \Lambda^{-1}(2 - \delta_{n,0}) \int_0^{\Lambda} \mathcal{H}_{x,m}^{\mathrm{II}}(x) \mathcal{H}_{x,n}^{\mathrm{III}}(x) dx,$$

$$
\begin{aligned}
\mathbf{H}_{n,m} = \Lambda^{-1}(2 - \delta_{n,0}) \{ & \{2\Lambda \cos(k_{s,m}s/2) \\
& \times [-2n\pi \cos(k_{a,m}a/2) \sin(an\pi/\Lambda) \\
& + k_{a,m}\Lambda \cos(an\pi/\Lambda) \sin(k_{a,m}a/2)]\}/(-4n^2\pi^2 + \Lambda^2 k_{a,m}^2) \\
& + \{\Lambda \cos(k_{a,m}a/2)[-2n\pi \cos(k_{s,m}s/2)[\sin(an\pi/\Lambda) \\
& + \sin(n\pi(a - 2\Lambda)/\Lambda)] \\
& - k_{s,m}\Lambda[\cos(an\pi/\Lambda) + \cos(n\pi(a - 2\Lambda)/\Lambda)] \\
& \times \sin(k_{s,m}s/2)]\}/(4n^2\pi^2 - \Lambda^2 k_{s,m}^2) \}.
\end{aligned}
\tag{A.3}
$$

$$\mathbf{E}_{n,m} = \Lambda^{-1}(2 - \delta_{n,0}) \left(\sqrt{\frac{\mu_0}{\varepsilon_0}}\right)^{-2} (-\gamma_n/k_0)^2 \int_0^\Lambda \mathcal{E}_{y,m}^{\mathrm{II}}(x) \mathcal{E}_{y,n}^{\mathrm{III}}(x) dx,$$

$$\begin{aligned}
\mathbf{E}_{n,m} = {} & \Lambda^{-1}\left(2 - \delta_{n,0}\right)\left(\gamma_n/\beta_m\right) \Big\{ \left\{ 2\Lambda \cos\left(k_{s,m}s/2\right) \right. \\
& \times \left[-2n\pi \cos\left(k_{a,m}a/2\right) \sin\left(an\pi/\Lambda\right) \right. \\
& \left. + \; k_{a,m}\Lambda \cos\left(an\pi/\Lambda\right) \sin\left(k_{a,m}a/2\right) \right] \Big\} / \left(-4n^2\pi^2 + \Lambda^2 k_{a,m}^2\right) \\
& + \Big\{ \Lambda \cos\left(k_{a,m}a/2\right) \left[-2n\pi \cos\left(k_{s,m}s/2\right) \left[\sin\left(an\pi/\Lambda\right) \right. \right. \\
& + \; \sin\left(n\pi\left(a - 2\Lambda\right)/\Lambda\right) \right] \\
& - k_{s,m}\Lambda[\cos\left(an\pi/\Lambda\right) + \cos\left(n\pi\left(a - 2\Lambda\right)/\Lambda\right)] \\
& \times \; \sin\left(k_{s,m}s/2\right) \Big] \Big\} / \left(4n^2\pi^2 - \Lambda^2 k_{s,m}^2\right) \Big\}. \quad (\mathrm{A}.4)
\end{aligned}$$

Acknowledgments

References and Notes

1. E. G. Loewen and E. Popov, *Diffraction Gratings and Applications* (CRC Press, 1997).
2. M. Born and E. Wolf, *Principles of Optics*, 7th (expanded) ed. (Cambridge University Press, 1999).
3. B. C. Kress and P. Meyrueis, *Applied Digital Optics: from Micro-optics to Nanophotonics* (Wiley, 2009).

4. C. F. R. Mateus, M. C. Y. Huang, Y. Deng, A. R. Neureuther, and C. J. Chang-Hasnain, "Ultra-broadband mirror using low index cladded subwavelength grating," IEEE Photon. Technol. Lett. **16**(2), 518–520 (2004).

5. C. J. Chang-Hasnain, C. F. R. Mateus, and M. C. Y. Huang, "Ultra broadband mirror using subwavelength grating," U.S. Patent 7,304,781 (Dec. 4, 2007).

6. S. Astilean, P. Lalanne, P. Chavel, E. Cambril, and H. Launois, "High-efficiency subwavelength diffractive element patterned in a high-refractive-index material for 633 nm," Opt. Lett. **23**(7), 552–554 (1998).

7. S. Goeman, S. Boons, B. Dhoedt, K. Vandeputte, K. Caekebeke, P. Van Daele, and R. Baets, "First demonstration of highly reflective and highly polarization selective diffraction gratings (GIRO-gratings) for long-wavelength VCSELs," IEEE Photon. Technol. Lett. **10**(9), 1205–1207 (1998).

8. T. Glaser, S. Schröter, H. Bartelt, H.-J. Fuchs, and E.-B. Kley, "Diffractive optical isolator made of high-efficiency dielectric gratings only," Appl. Opt. **41**(18), 3558–3566 (2002).

9. D. Rosenblatt, A. Sharon, and A. A. Friesem, "Resonant grating waveguide structures," IEEE J. Quantum Electron. **33**(11), 2038–2059 (1997).

10. R. Magnusson and S. S. Wang, "New principle for optical filters," Appl. Phys. Lett. **61**(9), 1022–1024 (1992).

11. A. Haglund, S. J. Gustavsson, J. Vukusic, P. Jedrasik, and A. Larsson, "High-power fundamental-mode and polarisation stabilised VCSELs using sub-wavelength surface grating," Electron. Lett. **41**(14), 805–807 (2005).

12. L. Zhuang, S. Schablitsky, R. C. Shi, and S. Y. Chou, "Fabrication and performance of thin amorphous Si subwavelength transmission grating for controlling vertical cavity surface emitting laser polarization," J. Vac. Sci. Technol. B **14**(6), 4055–4057 (1996).

13. C. F. R. Mateus, M. C. Y. Huang, L. Chen, C. J. Chang-Hasnain, and Y. Suzuki, "Broad-band mirror (1.12–1.62 μm) using a subwavelength grating," IEEE Photon. Technol. Lett. **16**(7), 1676–1678 (2004).

14. M. C. Y. Huang, Y. Zhou, and C. J. Chang-Hasnain, "A surface-emitting laser incorporating a high index-contrast subwavelength grating," Nat. Photonics **1**(2), 119–122 (2007).

15. Y. Zhou, M. C. Y. Huang, and C. J. Chang-Hasnain, "Large fabrication tolerance for VCSELs using high contrast grating," IEEE Photon. Technol. Lett. **20**(6), 434–436 (2008).

16. M. C. Y. Huang, Y. Zhou, and C. J. Chang-Hasnain, "A nanoelectromechanical tunable laser," Nat. Photonics **2**(3), 180–184 (2008).

17. C. Chase, Y. Zhou, and C. J. Chang-Hasnain, "Size effect of high contrast gratings in VCSELs," Opt. Express **17**(26), 24002–24007 (2009).

18. C. J. Chang-Hasnain, Y. Zhou, M. C. Y. Huang, and C. Chase, "High-contrast grating VCSELs," IEEE J. Sel. Top. Quantum Electron. **15**(3), 869–878 (2009).

19. C. Chase, Y. Rao, W. Hofmann, and C. J. Chang-Hasnain, "1550 nm high contrast grating VCSEL," Opt. Express **18**(15), 15461–15466 (2010).

20. W. Hofmann, C. Chase, M. Müller, Y. Rao, C. Grasse, G. Böhm, M.-C. Amann, and C. J. Chang-Hasnain, "Long-wavelength high-contrast

grating vertical-cavity surface-emitting laser," IEEE Photonics J. **2**(3), 415–422 (2010).

21. P. Gilet, N. Olivier, P. Grosse, K. Gilbert, A. Chelnokov, I.-S. Chung, and J. Mørk, "High-index-contrast subwavelength grating VCSEL," Proc. SPIE **7615**, 76150J (2010).

22. S. Boutami, B. Ben Bakir, J.-L. Leclercq, and P. Viktorovitch, "Compact and polarization controlled 1.55 μm vertical-cavity surface emitting laser using single-layer photonic crystal mirror," Appl. Phys. Lett. **91**(7), 071105 (2007).

23. S. Boutami, B. Benbakir, X. Letartre, J. L. Leclercq, P. Regreny, and P. Viktorovitch, "Ultimate vertical checkerboard–Perot cavity based on single-layer photonic crystal mirrors," Opt. Express **15**(19), 12443–12449 (2007).

24. I.-S. Chung, J. Mørk, P. Gilet, and A. Chelnokov, "Subwavelength grating-mirror VCSEL with a thin oxide gap," IEEE Photon. Technol. Lett. **20**(2), 105–107 (2008).

25. Y. Rao, C. Chase, and C. J. Chang-Hasnain, "Multiwavelength HCG–VCSEL Array," in *2010 Second IEEE International Semiconductor Laser Conference (ISLC)* (IEEE, 2010), pp. 11–12.

26. Y. Rao, C. Chase, M. C. Y. Huang, S. Khaleghi, M. R. Chitgarha, M. Ziyadi, D. P. Worland, A. E. Willner, and C. J. Chang-Hasnain, "Continuous tunable 1550-nm high contrast grating VCSEL," in *CLEO: Applications and Technology*, OSA Technical Digest (online) (Optical Society of America, 2012), paper CTh5C.3.

27. C. Sciancalepore, B. B. Bakir, X. Letartre, J. Harduin, N. Olivier, C. Seassal, J. Fedeli, and P. Viktorovitch, " CMOS-compatible ultra-compact 1.55-μm emitting VCSELs using double photonic crystal mirrors," IEEE Photon. Technol. Lett. **24**(6), 455–457 (2012).

28. T. Stöferle, N. Moll, T. Wahlbrink, J. Bolten, T. Mollenhauer, U. Scherf, and R. F. Mahrt, "Ultracompact silicon/polymer laser with an absorption-insensitive nanophotonic resonator," Nano Lett. **10**(9), 3675–3678 (2010).

29. F. Brückner, D. Friedrich, T. Clausnitzer, M. Britzger, O. Burmeister, K. Danzmann, E. B. Kley, A. Tünnermann, and R. Schnabel, "Realization of a monolithic high-reflectivity cavity mirror from a single silicon crystal," Phys. Rev. Lett. **104**(16), 163903 (2010).

30. Y. Zhou, M. Moewe, J. Kern, M. C. Y. Huang, and C. J. Chang-Hasnain, "Surface-normal emission of a high-*Q* resonator using a subwavelength high-contrast grating," Opt. Express **16**(22), 17282–17287 (2008).

31. V. Karagodsky, T. Tran, M. Wu, and C. J. Chang-Hasnain, "Double-resonant enhancement of surface enhanced Raman scattering using high contrast grating resonators," in *CLEO:2011—Laser Applications to Photonic Applications*, OSA Technical Digest (CD) (Optical Society of America, 2011), paper CFN1.

32. V. Karagodsky, B. Pesala, C. Chase, W. Hofmann, F. Koyama, and C. J. Chang-Hasnain, "Monolithically integrated multi-wavelength VCSEL arrays using high-contrast gratings," Opt. Express **18**(2), 694–699 (2010).

33. F. Lu, F. G. Sedgwick, V. Karagodsky, C. Chase, and C. J. Chang-Hasnain, "Planar high-numerical-aperture low-loss focusing reflectors and lenses using subwavelength high contrast gratings," Opt. Express **18**(12), 12606–12614 (2010).

34. D. Fattal, J. Li, Z. Peng, M. Fiorentino, and R. G. Beausolei, "Flat dielectric grating reflectors with focusing abilities," Nat. Photonics **4**(7), 466–470 (2010).

35. D. Fattal, J. Li, Z. Peng, M. Fiorentino, and R. G. Beausoleil, "A silicon lens for integrated free-space optics," in *Integrated Photonics Research, Silicon and Nanophotonics*, OSA Technical Digest (CD) (Optical Society of America, 2011).

36. Y. Zhou, V. Karagodsky, B. Pesala, F. G. Sedgwick, and C. J. Chang-Hasnain, "A novel ultra-low loss hollow-core waveguide using subwavelength high-contrast gratings," Opt. Express **17**(3), 1508–1517 (2009).

37. W. Yang, J. Ferrara, K. Grutter, A. Yeh, C. Chase, Y. Yue, A. E. Willner, M. C. Wu, and C. J. Chang-Hasnain, "Low loss hollow-core waveguide on a silicon substrate," Nanophotonics **1**(1), 23–29 (2012).

38. T. Sun, W. Yang, V. Karagodsky, W. Zhou, and C. Chang-Hasnain, "Low-loss slow light inside high contrast grating waveguide," Proc. SPIE **8270**, 82700A (2012).

39. B. Pesala, V. Karagodsky, and C. J. Chang-Hasnain, "Ultra-compact optical coupler and splitter using high-contrast grating hollow-core waveguide," in *Silicon and Nanophotonics*, OSA Technical Digest (CD) (Optical Society of America, 2010), paper IWH1.

40. L. Zhu, V. Karagodsky, and C. Chang-Hasnain, "Novel high efficiency vertical to in-plane optical coupler," Proc. SPIE **8270**, 82700L (2012).

41. M. G. Moharam and T. K. Gaylord, "Rigorous coupled wave analysis of planar grating diffraction," J. Opt. Soc. Am. **71**(7), 811–818 (1981).

42. S. T. Peng, "Rigorous formulation of scattering and guidance by dielectric grating waveguides: general case of oblique incidence," J. Opt. Soc. Am. A **6**(12), 1869 (1989).

43. L. Li, "A modal analysis of lamellar diffraction gratings in conical mountings," J. Mod. Opt. **40**(4), 553–573 (1993).

44. V. Karagodsky, F. G. Sedgwick, and C. J. Chang-Hasnain, "Theoretical analysis of subwavelength high contrast grating reflectors," Opt. Express **18**(16), 16973–16988 (2010).

45. V. Karagodsky, C. Chase, and C. J. Chang-Hasnain, "Matrix Fabry–Perot resonance mechanism in high-contrast gratings," Opt. Lett. **36**(9), 1704–1706 (2011).

46. V. Karagodsky and C. J. Chang-Hasnain, "Physics of near-wavelength high contrast gratings," Opt. Express **20**(10), 10888–10895 (2012).

47. P. Lalanne, J. P. Hugonin, and P. Chavel, "Optical properties of deep lamellar gratings: a coupled Bloch-mode insight," J. Lightwave Technol. **24**(6), 2442–2449 (2006).

48. T. Tamir, G. Griffel, and H. L. Bertoni, ed., *Guided-Wave Optoelectronics*, 2nd ed. (Springer-Verlag, 1990).

49. P. C. Magnusson, G. C. Alexander, V. K. Tripathi, and A. Weisshaar, *Transmission Lines and Wave Propagation*, 4th ed. (CRC Press, 2001).

50. C. Weisbuch, M. Nishioka, A. Ishikawa, and Y. Arakawa, "Observation of the coupled exciton-photon mode splitting in a semiconductor quantum microcavity," Phys. Rev. Lett. **69**(23), 3314–3317 (1992).

51. J. P. Reithmaier, G. Sęk, A. Löffler, C. Hofmann, S. Kuhn, S. Reitzenstein, L. V. Keldysh, V. D. Kulakovskii, T. L. Reinecke, and A. Forchel, "Strong coupling in a single quantum dot-semiconductor microcavity system," Nature **432**(7014), 197–200 (2004).

52. W. Shan, W. Walukiewicz, J. W. Ager III, E. E. Haller, J. F. Geisz, D. J. Friedman, J. M. Olson, and S. R. Kurtz, "Band anticrossing in GaInNAs alloys," Phys. Rev. Lett. **82**(6), 1221–1224 (1999).

53. D. J. Joannopoulos, S. G. Johnson, J. N. Winn, and R. D. Meade, *Photonic Crystals: Molding the Flow of Light*, 2nd ed. (Princeton University Press, 2008).

54. W. M. J. Green, M. J. Rooks, L. Sekaric, and Y. A. Vlasov, "Optical modulation using anti-crossing between paired amplitude and phase resonators," Opt. Express **15**(25), 17264–17272 (2007).

55. S. Fan, W. Suh, and J. D. Joannopoulos, "Temporal coupled-mode theory for the Fano resonance in optical resonators," J. Opt. Soc. Am. A **20**(3), 569–572 (2003).

56. K. Iga, "Surface-emitting laser-its birth and generation of new optoelectronics field," IEEE J. Sel. Top. Quantum Electron. **6**(6), 1201–1215 (2000).

57. F. Koyama, H. Uenohara, T. Sakaguchi, and K. Iga, "GaAlAs/GaAs MOCVD growth for surface emitting laser," Jpn. J. Appl. Phys. Part 1 **26**(Part 1, No. 7), 1077–1081 (1987).

58. J. L. Jewell, S. L. McCall, Y. H. Lee, A. Scherer, A. C. Gossard, and J. H. English, "Lasing characteristics of GaAs microresonators," Appl. Phys. Lett. **54**(15), 1400–1402 (1989).

59. L. A. Coldren, R. S. Geels, S. W. Corzine, and J. W. Scott, "Efficient vertical-cavity lasers," Opt. Quantum Electron. **24**(2), S105–S119 (1992).

60. M. Orenstein, A. Von Lehmen, C. J. Chang-Hasnain, N. G. Stoffel, J. P. Harbison, and L. T. Florez, "Matrix addressable vertical cavity surface emitting laser array," Electron. Lett. **27**(5), 437–438 (1991).

61. C. J. Chang-Hasnain, J. P. Harbison, C. E. Zah, M. W. Maeda, L. T. Florez, N. G. Stoffel, and T. P. Lee, "Multiple wavelength tunable surface emitting laser arrays," IEEE J. Quantum Electron. **27**(6), 1368–1376 (1991).

62. C. J. Chang-Hasnain, J. P. Harbison, G. Hasnain, A. Von Lehmen, L. T. Florez, and N. G. Stoffel, "Dynamic, polarization, and transverse mode characteristics of vertical cavity surface emitting lasers," IEEE J. Quantum Electron. **27**(6), 1402–1409 (1991).

63. M. W. Maeda, C. J. Chang-Hasnain, C. Lin, J. S. Patel, H. A. Johnson, and J. A. Walker, "Use of a multiwavelength surface-emitting laser array in a four-channel wavelength-division-multiplexed system experiment," Photonics Technol. Lett. **3**(3), 268–269 (1991).

64. K. H. Hahn, M. R. Tan, and S. Y. Wang, "Intensity noise of large area vertical cavity surface emitting lasers in multimode optical fibre links," Electron. Lett. **30**(2), 139–140 (1994).

65. C. J. Chang-Hasnain, "VCSEL for metro communications," in *Optical Fiber Communications*, , I. Kaminow and T. Li, eds. (Academic, 2002), vol. IV A, pp. 666–698.

66. M. Ortsiefer, R. Shau, G. Böhm, F. Köhler, and M. C. Amann, "Low-threshold index-guided 1.5 μm long-wavelength vertical-cavity surface-emitting laser with high efficiency," Appl. Phys. Lett. **76**(16), 2179 (2000).

67. N. Nishiyama, C. Caneau, B. Hall, G. Guryanov, M. Hu, X. Liu, M. Li, R. Bhat, and C. Zah, "Long-wavelength vertical-cavity surface-emitting lasers on InP with lattice matched AlGaInAs-InP DBR grown by MOCVD," IEEE J. Sel. Top. Quantum Electron. **11**(5), 990–998 (2005).

68. A. Syrbu, A. Mereuta, A. Mircea, A. Caliman, V. Iakovlev, C. Berseth, G. Suruceanu, A. Rudra, E. Deichsel, and E. Kapon, "1550 nm-band VCSEL 0.76 mW singlemode output power in 20–80°C temperature range," Electron. Lett. **40**(5), 306 (2004).

69. W. Yuen, G. S. Li, R. F. Nabiev, J. Boucart, P. Kner, R. J. Stone, D. Zhang, M. Beaudoin, T. Zheng, C. He, K. Yu, M. Jansen, D. P. Worland, and C. J. Chang-Hasnain, "High-performance 1.6 μm single-epitaxy top-emitting VCSEL," Electron. Lett. **36**(13), 1121–1123 (2000).

70. A. Mizutani, N. Hatori, N. Nishiyama, F. Koyama, and K. Iga, "In-GaAs/GaAs vertical-cavity surface emitting laser on GaAs (311)B substrate using carbon auto-doping," Jpn. J. Appl. Phys. **37**(Part 1, No. 3B), 1408–1412 (1998).

71. S. J. Schablitsky, L. Zhuang, R. C. Shi, and S. Y. Chou, "Controlling polarization of vertical-cavity surface-emitting lasers using amorphous silicon subwavelength transmission gratings," Appl. Phys. Lett. **69**(1), 7–9 (1996).

72. J. M. Ostermann, P. Debernardi, and R. Michalzik, "Optimized integrated surface grating design for polarization-stable VCSELs," IEEE J. Quantum Electron. **42**(7), 690–698 (2006).

73. A. Haglund, J. S. Gustavsson, J. Bengtsson, P. Jedrasik, and A. Larsson, "Design and evaluation of fundamental-mode and polarization-stabilized VCSELs with a subwavelength surface grating," IEEE J. Quantum Electron. **42**(3), 231–240 (2006).

74. R. Michalzik, J. M. Ostermann, and P. Debernardi, "Polarization-stable monolithic VCSELs," Proc. SPIE, **6908**, 69080A (2008).

75. S. Nakagawa, E. Hall, G. Almuneau, J. K. Kim, D. A. Buell, H. Kroemer, and L. A. Coldren, "88°C, continuous-wave operation of apertured, intra-cavity contacted, 1.55 μm vertical-cavity surface-emitting lasers," Appl. Phys. Lett. **78**(10), 1337 (2001).

76. W. Hofmann, E. Wong, G. Böhm, M. Ortsiefer, N. H. Zhu, and M. C. Amann, "1.55 μm VCSEL arrays for high-bandwidth WDM-PONs," IEEE Photon. Technol. Lett. **20**(4), 291–293 (2008).

77. M. Lackner, M. Schwarzott, F. Winter, B. Kogel, S. Jatta, H. Halbritter, and P. Meissner, "CO and CO_2 spectroscopy using a 60 nm broadband tunable MEMS–VCSEL at 1.55 μm," Opt. Lett. **31**(21), 3170–3172 (2006).

78. C. J. Chang-Hasnain, "Tunable VCSEL," IEEE J. Sel. Top. Quantum Electron. **6**(6), 978–987 (2000).

79. M. S. Wu, E. C. Vail, G. S. Li, W. Yuen, and C. J. Chang-Hasnain, "Widely and continuously tunable micromachined resonant cavity detector with wavelength tracking," IEEE Photon. Technol. Lett. **8**(1), 98–100 (1996).

80. D. Sun, W. Fan, P. Kner, J. Boucart, T. Kageyama, D. Zhang, R. Pathak, R. F. Nabiev, and W. Yuen, "Long wavelength-tunable VCSELs with optimized MEMS bridge tuning structure," IEEE Photon. Technol. Lett. **16**(3), 714–716 (2004).

81. F. Riemenschneider, M. Maute, H. Halbritter, G. Boehm, M. C. Amann, and P. Meissner, "Continuously tunable long-wavelength MEMS–VCSEL with over 40-nm tuning range," IEEE Photon. Technol. Lett. **16**(10), 2212–2214 (2004).

82. M. C. Y. Huang, K. B. Cheng, Y. Zhou, B. Pesala, C. J. Chang-Hasnain, and A. P. Pisano, "Demonstration of piezoelectric actuated GaAs-based

MEMS tunable VCSEL," IEEE Photon. Technol. Lett. **18**(10), 1197–1199 (2006).

83. B. Kögel, H. Halbritter, S. Jatta, M. Maute, G. Böhm, M.-C. Amann, M. Lackner, M. Schwarzott, F. Winter, and P. Meissner, "Simultaneous spectroscopy of NH_3 and CO using a >50 nm continuously tunable MEMS–VCSEL," IEEE Sens. J. **7**(11), 1483–1489 (2007).

84. H. Halbritter, C. Sydlo, B. Kögel, F. Riemenschneider, H. L. Hartnagel, and P. Meissner, "Impact of micromechanics on the linewidth and chirp performance of MEMS–VCSELs," IEEE J. Sel. Top. Quantum Electron. **13**(2), 367–373 (2007).

85. S. Jatta, B. Kögel, M. Maute, K. Zogal, F. Riemenschneider, G. Böhm, M.-C. Amann, and P. Meißner, "Bulk-micromachined VCSEL at 1.55 µm with 76-nm single-mode continuous tuning range," IEEE Photon. Technol. Lett. **21**(24), 1822–1824 (2009).

86. C. Chang-Hasnain, M. Maeda, N. Stoffel, J. Harbison, L. Florez, and J. Jewell, "Surface emitting laser arrays with uniformly separated wavelengths," Electron. Lett. **26**(13), 940–941 (1990).

87. L. E. Eng, K. Bacher, W. Yuen, J. S. Harris Jr., and C. J. Chang-Hasnain, "Multiple wavelength vertical cavity laser arrays on patterned substrates," IEEE J. Quantum Electron. **1**(2), 624–628 (1995).

88. F. Koyama, T. Mukaihara, Y. Hayashi, N. Ohnoki, N. Hatori, and K. Iga, "Wavelength control of vertical cavity surface-emitting lasers by using nonplanar MOCVD," IEEE Photon. Technol. Lett. **7**(1), 10–12 (1995).

89. T. Wipiejewski, M. Peters, E. Hegblom, and L. Coldren, "Vertical-cavity surface-emitting laser diodes with post-growth wavelength adjustment," IEEE Photon. Technol. Lett. **7**(7), 727–729 (1995).

90. D. K. Armani, T. J. Kippenberg, S. M. Spillane, and K. J. Vahala, "Ultra-high-Q toroid microcavity on a chip," Nature **421**(6926), 925–928 (2003).

91. T. Asano, B.-S. Song, Y. Akahane, and S. Noda, "Ultrahigh-Q nanocavities in two-dimensional photonic crystal slabs," IEEE J. Sel. Top. Quantum Electron. **12**, 1121–1134 (2006).

92. D. Ohnishi, T. Okano, M. Imada, and S. Noda, "Room temperature continuous wave operation of a surface-emitting two-dimensional photonic crystal diode laser," Opt. Express **12**(8), 1562–1568 (2004).

93. W.-H. Chang, W.-Y. Chen, H.-S. Chang, T.-P. Hsieh, J.-I. Chyi, and T.-M. Hsu, "Efficient single-photon sources based on low-density quantum dots in photonic-crystal nanocavities," Phys. Rev. Lett. **96**(11), 117401 (2006).

94. H. Takano, Y. Akahane, T. Asano, and S. Noda, "In-plane-type channel drop filter in a two-dimensional photonic crystal slab," Appl. Phys. Lett. **84**(13), 2226–2228 (2004).

95. E. Chow, A. Grot, L. W. Mirkarimi, M. Sigalas, and G. Girolami, "Ultracompact biochemical sensor built with two-dimensional photonic crystal microcavity," Opt. Lett. **29**(10), 1093–1095 (2004).

96. J. Niehusmann, A. Vörckel, P. H. Bolivar, T. Wahlbrink, W. Henschel, and H. Kurz, "Ultrahigh-quality-factor silicon-on-insulator microring resonator," Opt. Lett. **29**(24), 2861–2863 (2004).

97. A. Löffler, J. Reithmaier, G. Sek, C. Hofmann, S. Reitzenstein, M. Kamp, and A. Forchel, "Semiconductor quantum dot microcavity pillars with high-quality factors and enlarged dot dimensions," Appl. Phys. Lett. **86**(11), 111105 (2005).

98. H. A. Haus and Y. Lai, "Narrow-band distributed feedback reflector design," J. Lightwave Technol. **9**(6), 754–760 (1991).

99. S. Nie and S. R. Emory, "Probing single molecules and single nanoparticles by surface-enhanced Raman scattering," Science **275**(5303), 1102–1106 (1997).

100. P. J. Schuck, D. P. Fromm, A. Sundaramurthy, G. S. Kino, and W. E. Moerner, "Improving the mismatch between light and nanoscale objects with gold bowtie nanoantennas," Phys. Rev. Lett. **94**(1), 017402 (2005).

101. D. C. Shaver and D. C. Flanders, "X-ray zone plates fabricated using electron-beam and x-ray lithography," J. Vac. Sci. Technol. **16**(6), 1626–1630 (1979).

102. K. Rastani, A. Marrakchi, S. F. Habiby, W. M. Hubbard, H. Gilchrist, and R. E. Nahory, "Binary phase Fresnel lenses for generation of two-dimensional beam arrays," Appl. Opt. **30**(11), 1347–1354 (1991).

103. T. Fujita, H. Nishihara, and J. Koyama, "Blazed gratings and Fresnel lenses fabricated by electron-beam lithography," Opt. Lett. **7**(12), 578–580 (1982).

104. M. Haruna, M. Takahashi, K. Wakahayashi, and H. Nishihara, "Laser beam lithographed micro-Fresnel lenses," Appl. Opt. **29**(34), 5120–5126 (1990).

105. T. Shiono, M. Kitagawa, K. Setsune, and T. Mitsuyu, "Reflection micro-Fresnel lenses and their use in an integrated focus sensor," Appl. Opt. **28**(16), 3434–3442 (1989).

106. T. Shiono and K. Setune, "Blazed reflection micro-Fresnel lenses fabricated by electron-beam writing and dry development," Opt. Lett. **15**(1), 84–86 (1990).

107. Yu. V. Troitski, "The energy conservation law for optical two-port devices," Opt. Spectrosc. **92**(4), 555–559 (2002).

108. S. Fan, J. D. Joannopoulos, J. N. Winn, A. Devenyi, J. C. Chen, and R. D. Meade, "Guided and defect modes in periodic dielectric waveguides," J. Opt. Soc. Am. B **12**(7), 1267–1272 (1995).

Connie Chang-Hasnain is the John R. Whinnery Chair Professor in the Electrical Engineering and Computer Sciences Department and Chair of the Nanoscale Science and Engineering Graduate Group at the University of California, Berkeley. She received her Ph.D. degree from the same department in 1987. Prior to joining the Berkeley faculty, Dr. Chang-Hasnain was a member of the technical staff at Bellcore (1987–1992) and an Assistant Professor (1992–1995) and Associate Professor (1995–1996) of Electrical Engineering at Stanford University. She is an Honorary Member of A.F. Ioffe Institute (Russia), Chang Jiang Scholar Endowed Chair at Tsinghua University (China), Visiting Professor of Peking University (China) and National Jiao Tung University (Taiwan). Professor Chang-Hasnain's research interests range from semiconductor optoelectronic devices to materials and physics, with current foci on nanophotonic materials and devices for chip-scale integrated optics. Prof. Chang-Hasnain has been honored with the IEEE David Sarnoff Award

(2011), the OSA Nick Holonyak, Jr., Award (2007), the IEEE LEOS William Streifer Award for Scientific Achievement (2003), and the Microoptics Award from Japan Society of Applied Physics (2009). She is a Fellow of the OSA, IEE, and IEEE. Additionally, she has been awarded with a National Security Science and Engineering Faculty Fellowship by the Department of Defense (2008), a Humboldt Research Award of the von Humboldt Foundation (2009), and a Guggenheim Memorial Foundation Fellowship (2009). Professor Chang-Hasnain was a member of the USAF Scientific Advisory Board and the Board on Assessment of NIST Programs, National Research Council. She has been active in professional societies and held several leadership positions, as a member of the IEEE LEOS Board of Governors and OSA Board of Directors. She has been the Editor-in-Chief of the *Journal of Lightwave Technology* since 2007.

Weijian Yang received the B.S. degree in electronics engineering and computer science from Peking University, Beijing, China, in 2008. Since 2008, he has been working toward the Ph.D. degree in electrical engineering at the University of California, Berkeley, under the supervision of Prof. Connie J. Chang-Hasnain. His research interests include high-contrast gratings, integrated photonics, vertical-cavity surface-emitting lasers, radio frequency photonics, and optical injection locking. Mr. Yang is a student member of the Optical Society of America (OSA) and the Institute of Electrical and Electronics Engineers (IEEE).